Carbon 226 (2024) 119226

Contents lists available at ScienceDirect

Carbon

journal homepage: www.elsevier.com/locate/carbon

Robust and durable superlubricity enabled by carboxylated graphene quantum dots in lubricated steel contacts

Irfan Nadeem [a,b], Matjaž Finšgar [c], Goran Dražić [d], Matjaž Malok [e], Ardian Morina [f], Mitjan Kalin [a,*]

[a] Laboratory for Tribology and Interface Nanotechnology, Faculty of Mechanical Engineering, University of Ljubljana, Bogišićeva 8, Ljubljana 1000, Slovenia
[b] CEMMPRE — Centre for Mechanical Engineering Materials and Processes, Department of Mechanical Engineering, University of Coimbra, Rua Luís Reis Santos, 3030-788 Coimbra, Portugal
[c] Faculty of Chemistry and Chemical Engineering, University of Maribor, Smetanova ulica 17, Maribor 2000, Slovenia
[d] Department of Materials Chemistry, National Institute of Chemistry, Hajdrihova ulica 19, Ljubljana 1000, Slovenia
[e] Solid State Physics Department, Jožef Stefan Institute, Jamova cesta 39, Ljubljana 1000, Slovenia
[f] School of Mechanical Engineering, University of Leeds, LS2 9JT, Leeds, UK

ARTICLE INFO

Keywords:
Graphene quantum dots
Superlubricity
Boundary lubrication
Aqueous glycerol
Green tribology
Steel

ABSTRACT

Achieving macroscale superlubricity on engineering steel by utilizing aqueous green lubricants has gained growing interest, given its substantial potential to reduce energy consumption and carbon footprint. However, maintaining superlubricity under diverse sliding conditions over a prolonged duration is a major obstacle for real-scale applications. Herein, we report that a robust and durable tribofilm enabled by a unique lubrication mechanism based on carboxylated graphene quantum dots (CGQDs) in aqueous glycerol triggers macroscale superlubricity in self-mated steel contacts. A dedicated intermittent test was designed to show the superlubricity's robustness and the ability of the tribofilm to adapt to a variety of relevant sliding conditions. Moreover, the boundary film provides an average coefficient of friction of around 0.007 and up to 69 % wear reduction (compared to the base lubricant), resulting in the maintenance of superlubricity at a real final contact pressure of 123 MPa, which increases the upper limit of the contact pressure compared to current aqueous-lubricated steel contacts. The new superlubricity mechanism was enabled by the chemical adsorption of the CGQDs onto the worn metal surface, coupled with the tribo-induced structural degradation and transformation of the CGQDs into layered graphitic structures that generate an adaptable low-shear interface. This work provides new insights into the role of chemical adsorption and structural transformation of CGQDs in achieving superlubricity and is an important step forward for implementing energy-efficient and green lubrication technologies for industrial applications.

1. Introduction

With rapid industrialization, friction and wear are becoming concerning issues, leading to substantial energy losses, resource depletion, and environmental pollution. It is estimated that friction costs roughly one-fifth of the annual global primary energy [1]. Therefore, in terms of the Sustainable Development Goals, it is crucial to mitigate energy losses and carbon footprints by utilizing green lubricants [2]. At this juncture, the concept of superlubricity has attracted a great deal of attention owing to its prospects for minimizing material loss and energy consumption [3]. Superlubricity refers to a near-zero friction between two sliding surfaces, with the coefficient of friction (COF) falling below 0.01 [4].

Several approaches have been employed in recent years to achieve superlubricity in solid and liquid-lubricated contacts [5]. Solid superlubricity was achieved using various two-dimensional materials [6–10] and heterostructures [11–13]. However, it is usually achieved at the nano- or microscale and is pertinent to strictly defined conditions, including incommensurable contact or a specific external environment such as a particular temperature, ultra-high vacuum, or dry nitrogen environment [5,14,15].

In contrast, liquid superlubricity has been demonstrated at the macroscale under ambient conditions with a variety of liquid lubricants with and without additives, for instance, aqueous glycerol with or without nanodiamonds [16–18], ionic liquids combined with aqueous

* Corresponding author.
E-mail address: mitjan.kalin@fs.uni-lj.si (M. Kalin).

https://doi.org/10.1016/j.carbon.2024.119226
Received 30 January 2024; Received in revised form 7 May 2024; Accepted 8 May 2024
Available online 9 May 2024

glycerol [19], ionic liquids containing carbon quantum dots or graphene oxide (GO) [20,21], and ethanediol containing GO [22], etc. Nevertheless, superlubricity is predominantly observed in specific contact pairs consisting of diamond-like-carbon coatings (DLC) or ceramics, such as steel/ta-C [23], Si_3N_4/sapphire [14,21,24], and DLC/DLC [25,26]. However, in self-mated steel contacts, the phenomenon of superlubricity is rarely observed or realized only at low final contact pressures or in a mixed-lubrication regime [16–19,27,28]. This is due to either a rigorous tribochemical reaction or the unavoidable wear of contact surfaces during the running-in phase, which leads to the low contact pressure and causes the transition from boundary to a mixed-lubrication regime. Furthermore, in most of these studies, the superlubricity was very susceptible to test parameters, external contaminants, and environmental factors (such as temperature, humidity, etc.). Even a slight alteration to these factors could disrupt the superlubricious layer, resulting in a loss of superlubricity. Therefore, maintaining liquid superlubricity over an extended period under varying operating conditions is necessary for practical applications, especially for steel, the most widely used engineering material in the industrial world.

Recently, a newly developed fluorescent material, graphene quantum dots (GQDs), has attracted interest in various scientific fields such as photocatalysis, bioimaging, lithium-ion batteries, solar cells, and light-emitting diodes [29]. Unlike their cousins, carbon dots (CDs), GQDs are considered a smaller version of graphene oxide and possess the advantage of graphene lattices inside their dots [30]. Due to their very small size (<10 nm), low toxicity, eco-friendliness, and good biocompatibility, they have attracted a lot of attention as environmentally friendly additives in liquid lubricants [24]. In addition, their surface has excess-oxygen-containing moieties, which improves their compatibility and dispersibility in aqueous lubricants [31]. Moreover, GQDs possess a superior embedding stability between surface micro-asperities due to their ultra-small size compared to conventional carbon-based nanomaterials such as graphene and carbon nanotubes, as the latter have a large size in the lateral direction (in the micrometre range) [32,33]. A recent study has elucidated the impact of size variation in GO nano-additives on tribological performance. Particularly, the GO nanoflakes with smaller lateral dimensions effectively improve surface wear by easily penetrating the contact surfaces and forming a protective tribofilm [34]. Recently, Liu et al. [24] demonstrated the potential of GQDs to provide superlubricity between a Si_3N_4/sapphire tribo-pair using graphene oxide quantum dots (GOGQDs) as an additive in aqueous ethylene glycol. The results show that the formation of a tribofilm containing GOGQDs shortens the running-in time and provides superlubricity with a 90 % reduction in the wear volume compared to ethylene glycol. The mechanisms suggested that the rolling and shearing effects of GOGQDs are responsible for the superlubricity. The rolling effect of carbon-based quantum dots has been reported several times in the literature [24,31,33,35]. However, most of these studies lack direct evidence of the rolling effect [24,31,35]. In addition to rolling, adsorption, polishing, and mending effects are proposed as being responsible for their excellent lubrication performance [24,31,35].

There is no evidence of long-lasting superlubricity under boundary conditions between steel contacts using GQDs-based nano-lubricants [24,28,31,35]. Additionally, a comprehensive understanding of the prevailing boundary-lubrication mechanisms, encompassing the physical and chemical attributes of GQDs in the realization of superlubricity between steel/steel contacts, is not yet well understood, and so requires further investigation.

Recent studies have demonstrated that lubricants with excessive carboxylic groups can improve the tribological performance and provide superlubricity in certain tribo-pairs [25,36–39]. It is believed that the carboxylic groups bind strongly to the metal atoms on the worn surface and facilitate the formation of a dense tribofilm, improving the boundary-lubrication performance [36,38]. A recent study by Sun et al. [39] demonstrated macroscale superlubricity in a steel/a-C contact using an aqueous 3-hydroxypropionic acid (3HPA) solution. They suggested that the synergistic hydration effect provided by the water molecules and the chemisorption of the 3HPA molecules onto the oxidized steel surface in the mono or bi-dentate configuration facilitates the realization of superlubricity. However, due to excessive steel-ball wear during the running-in phase and the severe tribochemical reaction, the final contact pressure during the superlubricity is low (i.e., 55.04 MPa) compared to the initial contact pressure (i.e., 700 MPa). Thus, achieving superlubricity with aqueous lubricants usually requires a long running-in period, leading to severe wear of the friction pair before reaching the superlubricity state. Chemical modification of liquid lubricants and the incorporation of nanoparticles in aqueous lubricants have proved to be advantageous in reducing the running-in phase before achieving superlubricity [21].

Inspired by the rapid adsorption and friction-reduction capabilities of carboxylic groups and considering the merits of GQDs, we investigated the macroscale superlubricity between self-mated steel contacts using carboxylated graphene quantum dots (CGQDs) as nano-additives in aqueous glycerol under various contact pressures and sliding speeds. The worn surfaces were analysed using state-of-the-art surface-characterization techniques, including Raman, X-ray photoelectron, and time-of-flight secondary-ion mass spectrometry, while a scanning transmission electron microscope was utilized to investigate the tribo-induced interfacial changes to elucidate the underlying superlubricity mechanism between the steel/steel contacts.

2. Experimental section

2.1. Materials

The contact pairs used in this study consisted of steel balls with a diameter of 10 mm and steel discs with a diameter of 25 mm. Both were made of AISI 52100/DIN 100Cr6 steel with a hardness of 760 $HV_{0.1}$, determined using a micro-hardness tester (Leitz Miniload, Wild Leitz GmbH, Wetzlar, Germany). The steel ball had a measured surface roughness (R_q) of 40 ± 3 nm, while the discs were ground and polished to obtain a mirror surface finish with an R_q of 10 ± 2 nm.

Carboxylated graphene quantum dots (CGQDs) with a purity of more than 80 % and size of less than 10 nm were obtained from XFNANO Materials Tech. Co. Ltd (Nanjing, China). As specified by the supplier, the CGQDs were prepared by direct pyrolysis and tuning the carbonization degree of citric acid [40,41]. Pure glycerol derived from palm oil with a purity better than 99.5 % was purchased from Sigma Aldrich (St. Louis, MO, USA). The aqueous glycerol solution (G_{aq}) was prepared by mixing pure glycerol (70 wt%) and demineralized water (30 wt%), followed by stirring at ambient temperature (WiseStir MSH-20D, Germany) for 30 min to ensure homogenization. This glycerol-to-water ratio was chosen carefully to lower the freezing point of G_{aq} from 17 °C to −37 °C [42], and to reduce the viscosity (i.e., 18.2 cP) to the 97.8 % less than pure glycerol [43], where both properties extending its potential applications. Furthermore, a higher concentration of glycerol is advantageous for preventing water evaporation due to predominant glycerol-glycerol hydrogen bonds [44], which strengthens interactions among molecules [16,18,44]. The aqueous solutions of CGQDs ($CGQDs_{aq}$) were prepared by adding four different concentrations of CGQDs (i.e., 0.01, 0.025, 0.05, and 0.1 wt%) to G_{aq} followed by ultrasonication using a bath sonicator (Sonis 4 GT, Entjernej, Slovenia).

2.2. Characterization of CGQDs

The morphologies and microstructures of the CGQDs were determined using a transmission electron microscope (TEM; FEI Tecnai, NL) and an atomic force microscope (AFM; Asylum research MFP 3D origin, UK). For this purpose, CGQDs were added to isopropanol and diluted to a concentration of 0.1 mg/mL, then dripped and dried, respectively, on a copper grid (for TEM) and silicon wafer (for AFM). The chemical composition and structure of the CGQDs were studied using an X-ray

photoelectron spectrometer (XPS; Kratos, Manchester, UK), whereas the presence of surface functional groups were investigated using attenuated total reflection Fourier-transform infrared spectrometry (ATR-FTIR; PerkinElmer Instruments, USA). The crystal structure of the CGQDs was determined by X-ray diffraction (XRD; D8/Advance, Bruker, Germany) with a Co K_α radiation source over a 2Θ range of 5–80° with a step size of 0.02° at room temperature. The UV–Vis spectrum of the $CGQDs_{aq}$ was recorded using a UV–Vis spectrophotometer (Hewlett-Packard-8453, Palo Alto, CA). In addition, a custom-made 100-W ultraviolet lamp with a wavelength of 365 nm was used to investigate the light-excitation properties of the CGQDs and to further confirm their structure. The structural unit of the CGQDs was determined using a confocal Raman spectrophotometer (alpha 300 RS, Witec, Germany) operating at a laser wavelength of 532 nm. Finally, the surface charge of the CGQDs was determined using a Zetasizer Nano ZS instrument (Malvern, United Kingdom) by measuring the zeta-potential. For this purpose, the CGQDs were dissolved in ethanol at a 0.1-mg/mL concentration for the measurement.

2.3. Friction experiments

The friction experiments were performed with a ball-on-disc configuration in a reciprocating mode using a universal micro-tribometer (UMT-2, Bruker, USA). Prior to the friction tests, both the balls and the discs were ultrasonically cleaned sequentially in heptane for 20 min and then in acetone for 5 min. 30 μL of the prepared $CGQDs_{aq}$ solution was introduced into the contact zone before the start of each test. At first, the friction tests were conducted using pure water, G_{aq}, and 0.1 wt% $CGQDs_{aq}$ at an applied normal load and sliding speed of 3.5 N and 0.1 m/s, respectively. These tribological parameters and the concentration of CGQDs were carefully selected based on the existing literature on ultra-low friction involving aqueous lubricants [16,18,32,33]. In addition, the performance of the $CGQDs_{aq}$ lubrication was evaluated between self-mated hydrogenated DLC contacts (a-C:H/a-C:H), which are considered chemically non-reactive surfaces [45]. The objective was to investigate the effectiveness of the physical structure of CGQDs in reducing friction. Afterwards, the friction tests were conducted with normal loads of 2, 3.5, 5, and 10 N, corresponding to initial contact pressures of 0.6, 0.7, 0.8, and 1 GPa, respectively, according to Hertz's contact theory (0.1 wt% $CGQDs_{aq}$ and 0.1 m/s). The effect of sliding speeds on the superlubricity behaviour was evaluated by varying them from 0.05 to 0.15 m/s under optimum load and CGQD concentration. Finally, the influence of varying the CGQD concentrations (i.e., 0.01, 0.025, 0.05, and 0.1 wt%) on the superlubricity behaviour was investigated by conducting friction tests at a normal applied load of 3.5 N and sliding speed of 0.1 m/s. All these experimental conditions were chosen to ensure severe boundary lubrication (see Note S1). All the friction tests were performed at room temperature with a relative humidity of 28–32 % and repeated three to five times to ensure reproducibility.

2.4. Start-stop friction tests to assess the durability and robustness of the lubricating film

To evaluate the stability of the superlubricity over an extended period and under different operating conditions (i.e., sliding speeds and loads), a series of friction tests were designed and executed by performing start-stop tests after a running-in phase. All these tests were performed without altering the horizontal position of the friction pair using 0.1 wt% of CGQDs under ambient conditions, in contrast to the controlled laboratory conditions.

2.5. Worn-surface analysis

After the friction experiments, the contact surfaces were thoroughly cleaned with isopropanol to remove contaminants on the worn surface prior to the subsequent characterization. The wear-scar diameter (WSD), surface roughness, and morphology of the worn surfaces were analysed using a 3D white-light interferometer (Bruker - Contour GT -K0, Germany) and a digital microscope (Hirox - HRX-01, Japan). The wear volume of the discs was difficult to determine because the surface is almost wear-less, and the surface-wear profile could not be accurately fitted into a reliable wear equation. Therefore, the wear volumes of the steel balls with effective WSD after the tribological tests were calculated using the following equation [46]:

$$V = \left(\frac{1}{6}\pi h\right)\left(\frac{3}{4}d^2 + h^2\right) \quad (1)$$

where,

$$h = r - \sqrt{r^2 - \frac{1}{4}d^2} \quad (2)$$

where d is the WSD, and r is the radius of the actual ball.

In addition, the topography of the worn surfaces was analysed using a scanning electron microscope (SEM; JEOL, JSM IT100) under a high vacuum. 2D Raman mapping on the wear track was performed with a WITec Alpha 300 RS (WITec, Ulm, Germany) scanning confocal Raman microscope equipped with a piezo stage in a backscattered geometry using a frequency-doubled Nd:YAG laser (532 nm).

The chemical composition of the worn surfaces was investigated using XPS and time-of-flight secondary-ion mass spectrometry (ToF-SIMS). The XPS measurements were performed with an AXIS Supra+ instrument (Kratos, Manchester, UK) equipped with an Al K_α (1486.6 eV) excitation source and a monochromator. The analyses were performed at a take-off angle of 90° (with respect to the surface of the samples), where the diameter of the analysed spot size in the wear track was 55 μm. The analysed spot size for the XPS measurements outside the wear track was 300 by 700 μm. A main peak at 284.8 eV in the high-resolution (HR) C 1s spectra was used to correct the binding energy (E_B) scale. ESCApe 1.4 software was used to acquire and process the data (Kratos, Manchester, UK). ToF-SIMS measurements were performed with an M6 instrument (IONTOF, Münster, Germany). Spectra in positive and negative polarity were calibrated using the signals of known m/z. The measurements were performed using a 30-keV Bi_3^+ primary beam (target current of 0.6 pA). Sputtering was performed using a gas-cluster ion beam (GCIB) at an acceleration energy of 5.0 keV and Ar_{1900}^+ on an area of 500 × 500 μm, while the analysis was performed on an area of 300 × 300 μm. ToF-SIMS data acquisition and processing were performed using SurfaceLab 7.3 software (IONTOF, Münster, Germany).

To study the tribo-induced interfacial changes, a TEM lamella was prepared from the worn surface using an in-situ lift-out technique with a combined focused ion beam (FIB) and SEM (Helios Nanolab 650, FEI, NL). Prior to the lamella preparation, a uniform Cr layer of about 30 nm was deposited on the surface, followed by the deposition of a Pt layer at the FIB cutting position to protect the underlying tribolayer during lamella preparation. A cross-sectional examination of the lamellae was then performed using a probe Cs aberration-corrected cold-field-emission-gun scanning transmission electron microscope (STEM; JEOL JEM, ARM 200-CF, JP) equipped with a Jeol Centurio EDS system with a 100-mm^2 SDD detector and operating at an accelerating voltage of 80 KV. Electron-energy-loss spectroscopy (EELS) was performed using the Gatan DualEEELS Quantum ER spectrometer to elucidate the bonding and compositional features of the tribofilm. Data acquisition and analysis of the STEM images and EELS spectra were performed using Digital Micrograph software (Gatan Inc., CA, USA).

3. Results

3.1. Characterization of CGQDs

The microstructure, morphology, and chemical nature of the CGQDs

impact the tribological performance and are characterized by TEM, AFM, Raman, XRD, ATR-FTIR, and XPS (Fig. 1). A TEM image of CGQDs shows that they have a spherical morphology and uniform size, ranging from 1 to 4 nm (Fig. 1a and b). The inset of Fig. 1a showed that they have an in-plane lattice spacing of 0.24 nm, which corresponds to the (1120) lattice plane of graphene [47,48]. The AFM image in Fig. 1c shows that the topographic height is not more than 1.5 nm, indicating that most CGQDs have 1–4 graphene layers inside their dots [49]. The X-ray diffraction pattern of the CGQDs in Fig. S1a showed a broad diffraction peak at ~28° corresponding to the (002) plane of the graphitic structure [48]; this broader peak is due to the super-small size of the CGQDs [50]. Raman spectroscopy was used to investigate the chemical structure of the CGQDs. The Raman spectrum in Fig. S1b shows the two characteristic peaks at ~1378 and ~1587 cm^{-1}, which correspond to the disordered D band (originating from a disorder of the carbon lattice due to an excess of oxygen-containing functional groups) and the graphitic G band (stemming from the sp^2 hybridized carbon lattice), respectively [51]. The intensity ratio (I_D/I_G) of these two bands is 0.88, indicating a defect-rich structure due to excessive functional groups on the surface of the CGQDs, which could serve as strong active sites for interactions with the worn metallic surface. The broadness of the D and G bands and the absence of a doublet between them indicate that the CGQDs are mainly composed of nanocrystalline graphite [52]. ATR-FTIR spectroscopy was used to identify the functional groups on the surfaces of the CGQDs. The ATR-FTIR spectrum in Fig. 1d shows the O–H stretching vibration at about 3400 cm^{-1} [53]. The peaks at 1710 and 1404 cm^{-1} correspond to the stretching of the C═O and C–O, respectively, confirming the presence of carboxylic acid groups [53,54]. Moreover, the peak at 1637 cm^{-1} is due to the bending vibrations of the aromatic C═C [22,55], while the peak at 1213 cm^{-1} corresponds to the C–OH stretching of the hydroxyl groups [53]. Next, an XPS analysis was performed to determine the chemical composition and to confirm the functional groups in the CGQDs further. The XPS survey spectrum in Fig. S2 shows that the CGQDs signals correspond to C 1s and O 1s, respectively. By performing a quantitative XPS analysis, a C concentration of 57.3 at.% and an O concentration of 42.7 at.% were obtained. Furthermore, a high resolution (HR) C 1s spectrum of CGQDs was deconvoluted with peaks following a Gaussian-Lorentzian function. The HR C 1s spectrum (Fig. 1e) was deconvoluted into three components, which correspond to C═C/C–C at an E_B of 284.8 eV (no attempt was made to separate the peaks for C–C and C═C as they appear very close together), C–O at 286.4 eV, and COO/COOH at an E_B of 288.6 eV [53]. UV–vis spectroscopic analyses were used to further characterize the CGQDs. The UV–vis absorption spectra show that the CGQDs exhibit a strong absorption peak at a wavelength of about 239 nm (Fig. 1f), corresponding to the π–π* transition in the carbon core [56]. While a long absorption edge at a wavelength of about 340 nm, originates from the n–π* transition of C═O bonds at the edges or in the carbogenic core [47]. The unpaired electrons on the oxygen in the C═O bond are referred to as nonbonding or 'n' electrons, and a transition from n to π* occurs when one of these electrons is excited to the antibonding π* orbital. The inset of Fig. 1f shows that the CGQDs emit a bright blue colour when irradiated with a UV light of 365 nm. This emission behaviour and the UV absorbance in the CGQDs are most likely due to the synergistic effect of the quantum-confinement effect and their surface-oxygenated state [57]. The dispersion stability of the $CGQDs_{aq}$ was further investigated by irradiating the lubricant under a UV lamp. The consistent and uniform emission of the blue colour from the lubricant shows that the CGQDs remain stable and uniform without aggregating, even after 6 months of preparation. These results indicate that CGQDs have smaller dimensions compared to graphene and graphene oxide. Additionally, they exhibit a graphene-layered structure within their dots, along with carboxylic functional groups on their surface. These combined attributes make CGQDs promising candidates for lubricant additives.

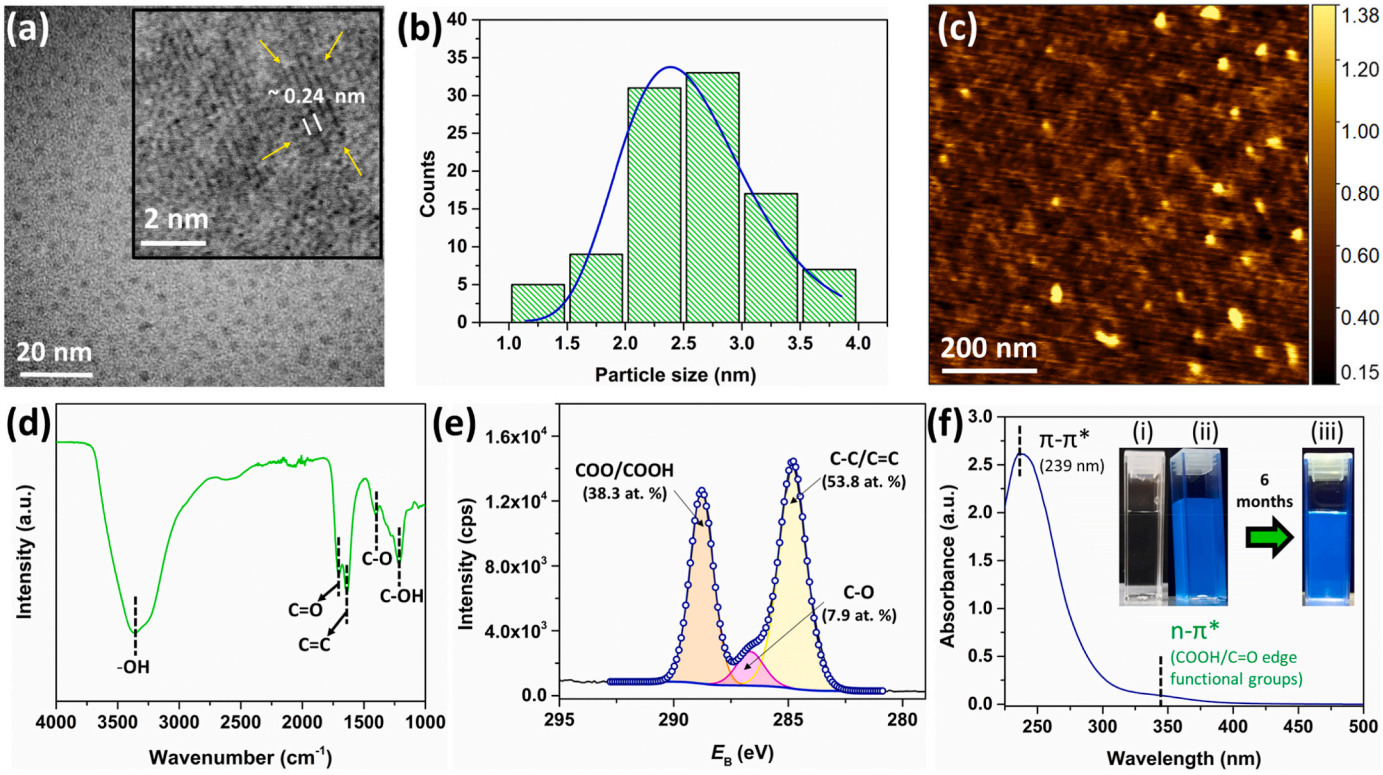

Fig. 1. Characterization of CGQDs: (a) TEM image (inset HR TEM image), (b) particle size distribution determined by TEM, (c) AFM analysis, (d) ATR-FTIR spectrum, (e) HR C 1s XPS spectrum, and (f) UV–Vis spectrum of CGQDs, where inset shows a photograph of 0.025 wt% $CGQDs_{aq}$ under (i) white light, (ii) UV light after sonication, and (iii) after standing for 6 months.

3.2. Macroscale superlubricity evaluation of CGQDs

The macroscale superlubricity behaviour of $CGQDs_{aq}$ under various contact pressures, sliding speeds, and for different concentrations is presented in Figs. 2 and 3. To demonstrate the significance of the CGQD nano-additives in aqueous glycerol (G_{aq}), additional friction tests were conducted with pure water and G_{aq} (Fig. 2a). For lubrication with pure water, the COF is relatively high, in the range ~0.3–0.33, indicating the ineffectiveness of the water to form a compelling lubricating film. In contrast, for lubrication with G_{aq}, the COF is about 0.058 during the first ~1000 s of the initial running-in period, then gradually begins to decrease, reaching a minimum value of ~0.028 by the end of the test, indicating the possible formation of a lubricating film by G_{aq}, but this film does not have superior characteristics to provide superlubricity. When lubricated with $CGQDs_{aq}$, the COF drops to a value below 0.01 shortly after ~620 s of the running-in period and then decreases to ~0.006 and remains stable until the end of the test, indicating a 72–78 % reduction in the COF compared to the G_{aq}. An additional friction test was performed with an old $CGQDs_{aq}$ (standing for 6 months after preparation) to evaluate the dispersion stability and efficacy of the $CGQDs_{aq}$. Fig. S3a shows that the old $CGQDs_{aq}$ maintained its lubricating performance and provided superlubricity, indicating that the CGQDs remain stable and uniform in aqueous glycerol for a long time without aggregating.

Next, the effectiveness of the $CGQDs_{aq}$ lubrication was evaluated between self-mated, hydrogenated diamond-like-carbon (a-C:H) contacts (Fig. 2b). In the case of self-mated a-C:H contacts, the superlubricity is not realized, and the COF decreases to ~0.015 after a long running-in period. Since the a-C:H coatings are regarded as a non-reactive surface [45], this decrease in friction could be attributed to a physical mechanism based on inter-layer shearing of the graphene layers within the CGQDs, suggesting that the structure of the CGQDs plays an important role in the friction reduction. In contrast, robust superlubricity is achieved in self-mated steel contacts, indicating the possible formation of a tribochemical film due to a tribochemical reaction.

The effect of varying the contact pressure on the superlubricity performance of $CGQDs_{aq}$ was further investigated by varying the applied normal loads (Fig. 2c). It was observed that for all the applied loads, the corresponding COF decreases to 0.006–0.0095 after the running-in phase, maintaining the state of superlubricity. When the contact pressure was increased from 0.6 to 0.7 GPa (2–3.5 N), the time to reach superlubricity slightly increased from 550 to 620 s, respectively. To evaluate the influence of low contact pressure on the running-in time, another friction test was conducted at 0.5 GPa (1.5 N), as shown in Fig. S3b. The result indicated that the running-in time was about the same as observed for 0.6 and 0.7 GPa. However, with a further increase in the contact pressure to 0.8 and 1 GPa (5 and 10 N), the time to reach the superlubricity state increased to ~1100 and ~1250 s, respectively. This increase in the running-in period could be due to the unavoidable wear of the contact surfaces with increasing contact pressure. This implies that the increasing contact pressure in our case does not prevent from achieving the superlubricity, but just increases the running-in time, and a stable superlubricity is observed between steel/steel contacts even at an initial contact pressure of 1 GPa.

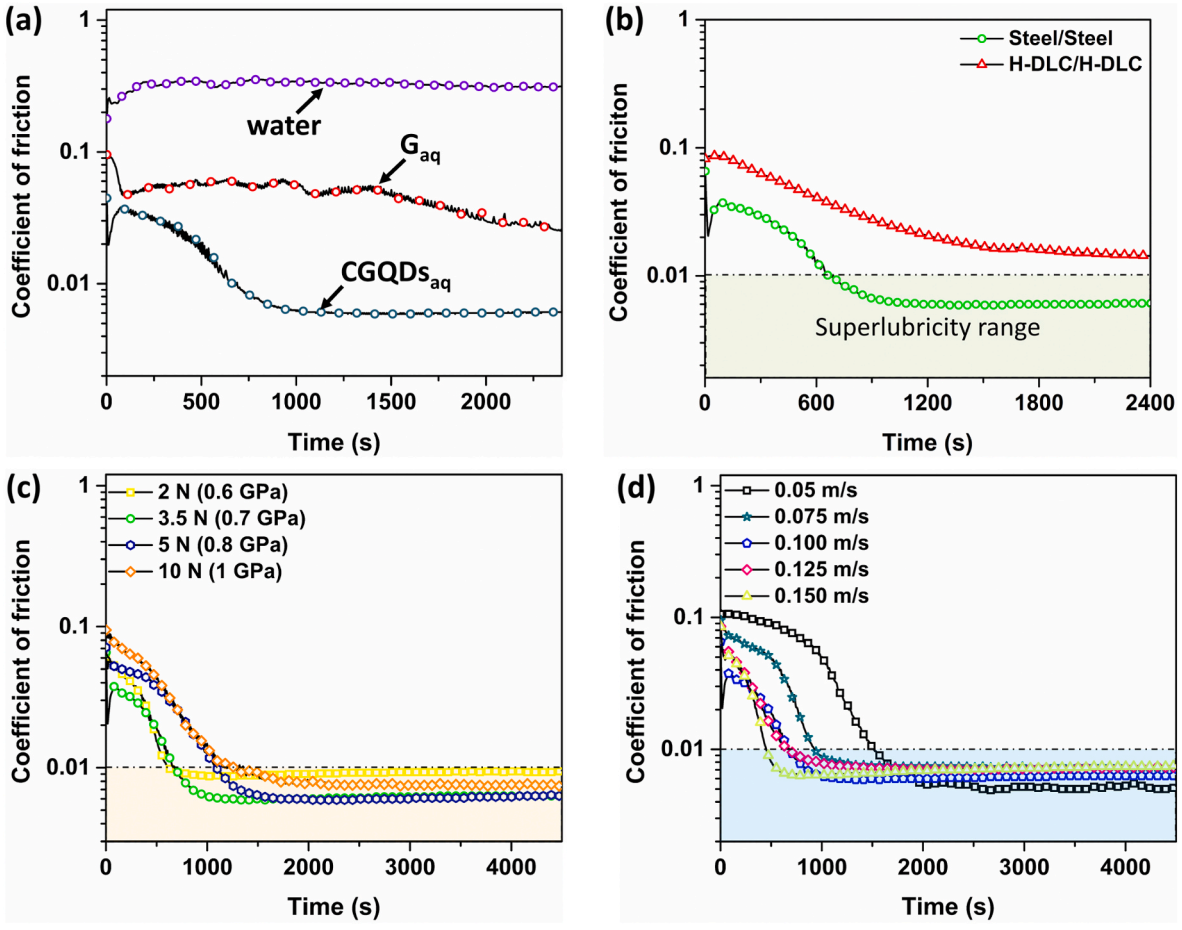

Fig. 2. Tribological characterization of $CGQDs_{aq}$: (a) Evolution of COF over time when lubricated with pure water, G_{aq}, and 0.1 wt% $CGQDs_{aq}$, respectively (test conditions: 3.5 N and 0.1 m/s). (b) Comparison of frictional performance of self-mated a-C:H and steel contacts lubricated with 0.1 wt% $CGQDs_{aq}$ (3.5 N and 0.1 m/s). (c) COFs as a function of time at various normal loads (2–10 N, 0.1 m/s), and (d) at various sliding speeds (0.05–0.15 m/s, 3.5 N) lubricated with 0.1 wt % $CGQDs_{aq}$.

The robustness of the superlubricity was further evaluated by varying the sliding speed from 0.05 to 0.15 m/s (Fig. 2d). It can be seen that as the sliding speed increases from 0.05 to 0.15 m/s, the time to reach the superlubricity state decreases from ~1517 to 453 s and the COF remains stable between 0.005 and 0.0075, with the lowest COF value (i.e., 0.005) being reached at a sliding speed of 0.05 m/s. The sliding distance required to reach the superlubricity state does not vary much and lies in the range ~63–81 *m*.

The influence of varying the CGQD concentration on the superlubricity behaviour and the final contact pressure (FCP) is shown in Fig. 3a. FCP refers to a contact pressure calculated over the final contact area, rather than the initial, theoretical nominal contact pressure, i.e., by dividing the normal applied load by the worn ball contact area [14,21]. With 0.01 wt% of CGQDs concentration, the friction is reduced by 54.5 % compared to the G_{aq}, achieving an average COF value of 0.011, which is close to the superlubricity range. Consequently, the WSD is reduced by 21.5 % (see Table S2), resulting in a 38 % increase in FCP compared to the G_{aq}, indicating the ability of CGQDs to reduce both friction and wear. This suggests that the 0.01 wt% of CGQDs is insufficient to form an effective lubricating film to realize the superlubricity. However, with a further increase in the concentration to 0.025 and 0.05 wt%, the average COF decreased to 0.006–0.007, while the corresponding FCP increased to 110–112 Mpa. However, when the concentration is increased to 0.1 wt%, superlubricity is also achieved, and the FCP increases to a maximum value of 123 MPa. These results imply that 0.01 wt% CGQDs is the threshold for attaining superlubricity, and when the concentration exceeds this threshold, robust superlubricity is achieved under the given experimental conditions.

Fig. 3b shows the influence of applied normal loads and sliding speeds on the FCP during the superlubricity state. The FCP increases with increasing applied normal load from 2 to 3.5 N (0.6–0.7 GPa), reaching a maximum value of 123 MPa, which means 112 % higher than G_{aq} (i.e., ~58 MPa). However, when the applied normal load is further increased from 3.5 to 10 N (0.7–1 GPa), the FCP fluctuates in the range 113–123 MPa. It can be seen that the FCP does not increase monotonically with an increase of the initial contact pressure. Whereas the initial contact pressure increases linearly (from 0.6 to 1 GPa) with an increasing applied normal load from 2 to 10 N, which could influence the wear behaviour during the running-in period. Therefore, the FCP is always lower than the initial contact pressure due to the unavoidable wear of the ball during the running-in period. In contrast, the FCP increases with an increasing sliding speed from 0.05 to 0.1 m/s, reaching a maximum value of 123 MPa. However, it slightly decreases to about 102 MPa with an increase in the sliding speed to 0.15 m/s. This means that for our conditions, 0.1 m/s is the optimum sliding speed for achieving superlubricity.

The results in Figs. 2 and 3 suggest that this realization of superlubricity is due to a specific lubrication mechanism rather than elasto-hydrodynamic lubrication. The superlubricity performance of the CGQDs as lubricant additives can be summarized as follows: (i) CGQDs provide superlubricity under various initial contact pressures (even at 1 GPa) and sliding speeds; (ii) robust superlubricity could be achieved with a concentration of CGQDs as low as 0.025 wt%, significantly reducing the costs associated with synthesizing nano-lubricants; (iii) the highest FCP during superlubricity is as high as 123 MPa in the boundary-lubrication regime, which is achieved at an initial contact pressure of 0.7 GPa, a sliding speed of 0.1 m/s, and with 0.1 wt% CGQDs.

3.3. Surface characterization of the worn surfaces

After the friction tests, the worn surfaces lubricated with $CGQDs_{aq}$ were characterized using a 3D white-light interferometer and an SEM (Fig. 4a and b). The wear-scar diameter (WSD) on the ball lubricated with $CGQDs_{aq}$ is about 186.5 μm, which is 35.2 % less than the WSD on the ball lubricated with G_{aq} (i.e., 287.7 μm). In addition, the surface roughness of the ball's wear scar lubricated with $CGQDs_{aq}$ was about 12.7 nm, which is about 3 times less than the original roughness of the ball (i.e., 40 nm). In contrast, the surface roughness was about 19.8 nm for the ball's wear scar when lubricated with G_{aq}, which was considerably larger than the surface lubricated with $CGQDs_{aq}$ (Fig. 4a). The surface topography of the disc lubricated with $CGQDs_{aq}$ indicates that the surface is relatively smooth compared to the surface lubricated with G_{aq}, with a maximum wear depth of only 15 nm, indicating the excellent wear-reduction ability of CGQDs. In contrast, the maximum wear depth was 105 nm when lubricated with G_{aq}. Therefore, it was difficult to calculate the wear volume of the discs because the surface-wear profile could not be accurately fitted into a reliable wear equation. Consequently, the effective WSDs of the steel balls after the friction test were used to estimate the wear volume using Equation (1). Fig. S3c shows the wear volume, and Table S2 shows the average WSD of the balls lubricated with $CGQDs_{aq}$ under different loads, sliding speeds, and CGQD concentrations. The average WSD decreases from 277.5 to 217.8 μm when the concentration of CGQD nano-additives increases from 0 to 0.01 wt%. However, when the CGQD concentration is further increased (i.e., 0.025–0.1 wt%), it does not vary much and ranges from 190.7 to 200.1 μm. In contrast, it increases from 171.2 to 326.9 μm with an increasing normal applied load from 2 to 10 N. This increase in WSD is due to the increase in the severity of the wear with the increasing load during the running-in period, resulting in an increase in wear volume to 11.6×10^{-5} mm^3, which is still a considerably lower value for the self-mated steel contacts under aqueous lubrication conditions (Fig. S3c). In contrast, with increasing sliding speed from 0.05 to 0.075 m/s, the WSD decreases from 285.3 to 224.7 μm, while it further decreases to an average value of 190.7 μm at a sliding speed of 0.1 m/s, resulting in a

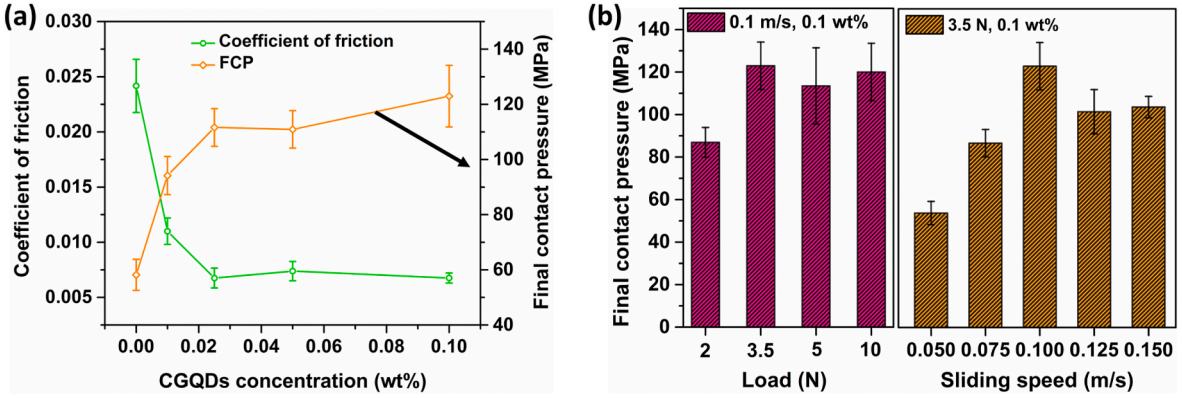

Fig. 3. (a) Average COFs and corresponding measured final contact pressures (FCP) during superlubricity with various concentrations of CGQD (3.5 N, 0.1 m/s). (b) The corresponding FCP in a superlubricity state with various loads and sliding speeds (conc. of CGQDs is 0.1 wt%), where the FCP is calculated by dividing the normal applied load by the contact area of the worn region on the ball.

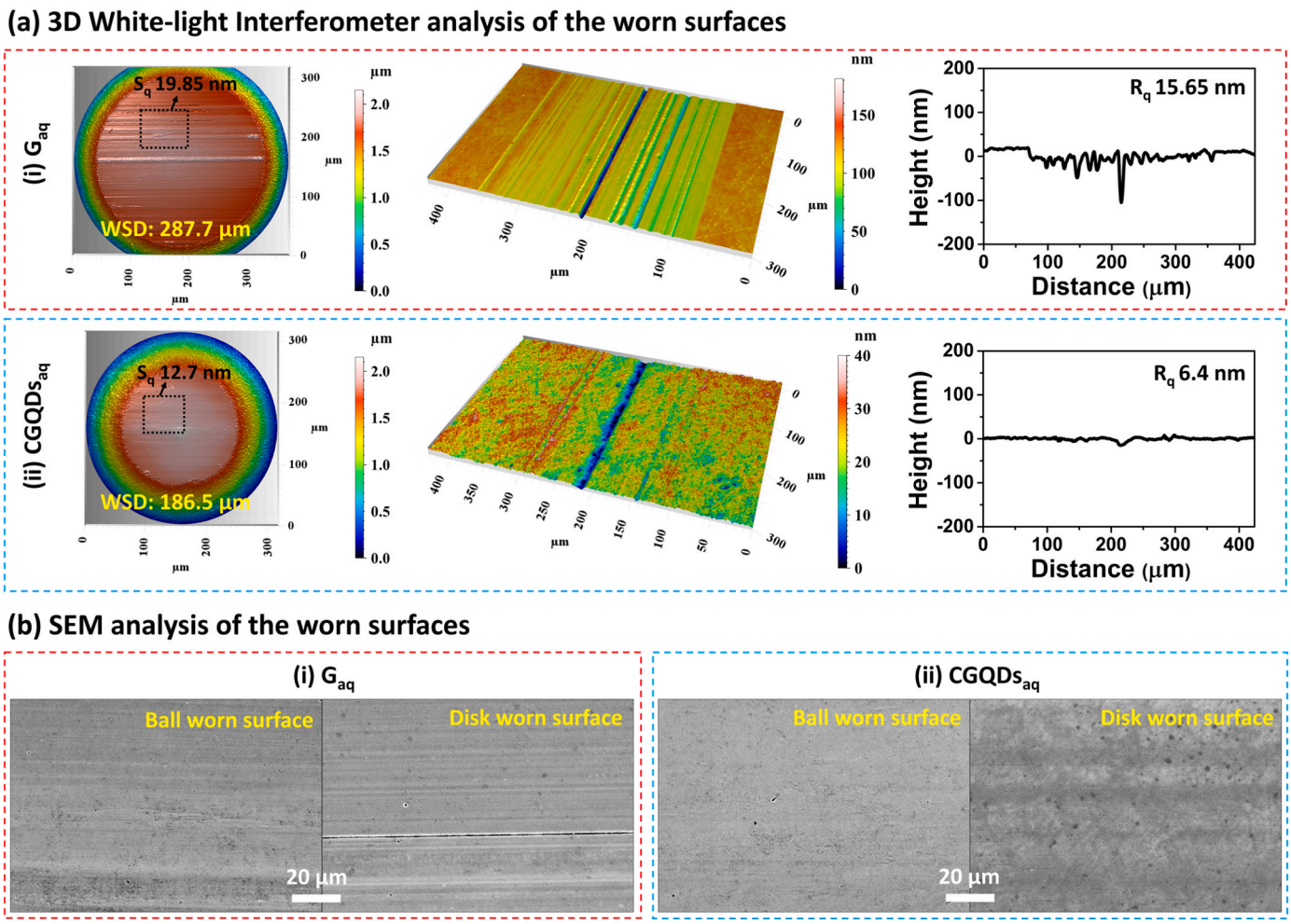

Fig. 4. Characterization of worn surfaces after friction tests with G_{aq} and 0.1 wt% $CGQDs_{aq}$ (3.5 N, 0.1 m/s): (a) 3D surface topography of the balls and the worn disc surfaces lubricated with (i) G_{aq}, and (ii) $CGQDs_{aq}$. (b) SEM images of the morphology of the worn surfaces lubricated with (i) G_{aq}, and (ii) $CGQDs_{aq}$.

minimum wear volume of 1.30×10^{-5} mm^3 (see Fig. S3c and Table S2). However, with a further increase in the sliding speed to 0.125 and 0.15 m/s, the WSD does not vary much and lies between 200 and 205 µm.

Next, the worn zone on the steel ball and the wear track on the steel disc after the friction test were analysed using the SEM (Fig. 4b). It can be seen that the worn surfaces (steel ball and disc) lubricated with G_{aq} are relatively rough and show some abrasion marks, compared to the surfaces lubricated with $CGQDs_{aq}$, which are much smoother and hardly show any sign of wear. This implies that the $CGQDs_{aq}$ protects the contact surfaces from severe wear, suggesting the formation of a protective tribofilm.

Raman mapping was used to investigate the adsorbed tribofilm on the worn surface of the disc (Fig. 5). Fig. 5b shows the Raman mapping of the signal intensity of the characteristic G band. The regions with a bright yellow colour correspond to the active Raman modes of the G band, indicating that the CGQDs are adsorbed onto the worn surface,

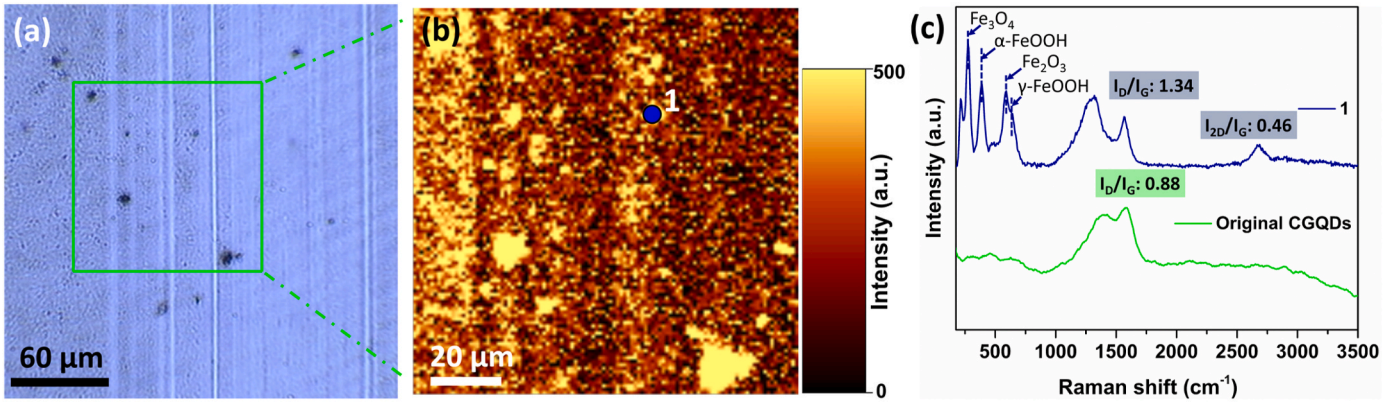

Fig. 5. Raman analysis of the worn disc surface after the friction test performed with 0.1 wt% $CGQDs_{aq}$; (a) optical image of the worn region, (b) Raman-intensity map of the G band in the spectral range 1490–1720 cm^{-1}, and (c) corresponding Raman spectrum obtained at a location marked in a 2D Raman map.

providing evidence for the formation of a tribofilm that is responsible for the superlubricity. The Raman spectrum obtained at point 1 shows the characteristic D, G, and 2D bands, corresponding to the graphitic carbon structure [51]. The variation of the intensity ratio of the D band to the G band (I_D/I_G) reflects the degree of disorder or structural defects in carbon-based materials [58,59]. The Raman spectrum shows that I_D/I_G increases from 0.88 ± 0.01 (for CGQDs) to 1.34 ± 0.02 after the tribological test (Fig. 5c), indicating the friction-induced structural deformation and degradation of the CGQDs. This increase in I_D/I_G could also be attributed to the additional defects in the carbon network of graphene resulting from the formation of C–H and C–OH bonds due to sliding in the presence of an aqueous lubricant [60]. Furthermore, a 2D band at ~2680 cm^{-1} and an I_{2D}/I_G ratio of 0.46 ± 0.01 indicate that the CGQDs in the adsorbed tribofilm have a multilayer structure. Nevertheless, the appearance of well-defined 2D and G bands implies the existence of a tribofilm with a graphite-like carbon structure [61]. Additionally, the multiple peaks observed below 750 cm^{-1}, correspond to iron oxide and hydroxide [62]. The peak and shoulder at about 590 and 655 cm^{-1} indicate the presence of Fe_2O_3 (hematite) and γ-FeOOH (lepidocrocite) [63]. While the peaks centred at ~274.2 and 383 cm^{-1} correspond to magnetite (Fe_3O_4) and α-FeOOH (goethite), respectively [62]. The presence of γ-FeOOH could be responsible for the polishing effect observed on the surfaces of the steel contact (see Fig. 4a), as explained by Long et al. [23].

The chemical composition on the worn surface lubricated with 0.1 wt % $CGQDs_{aq}$ was analysed by XPS after the 75-min friction test (3.5 N, 0.1 m/s), where the analysed spot size inside the wear track was 55 μm. The surface atomic concentration of C-, O-, and Fe-containing species was determined to be 41.0, 44.3, and 14.7 at. %, respectively. The HR C 1s spectrum inside and outside of the wear track indicates the presence of four peaks centred at E_B of 283.0, 284.8, 286.4, and 288.6 eV, which corresponds to C–Fe, C═C/C–C, C–O, and COO/COOH, respectively (Fig. 6a and b). Compared with the HR C 1s spectra of the original CGQDs (Fig. 1e), the surface atomic concentration of C in the C–O increased to 16.3 at. %, whereas the surface atomic concentration of C in COO/COOH decreased from 38.3 to 30.8 at. %. Therefore, the density of carbon-containing groups was changed under sliding. This could be due to the tribochemical interaction of the CGQDs with the worn steel surface. Interestingly, there is no significant difference in the concentration of C═C/C–C, which indicates that the structure of CGQDs is not completely damaged due to friction [33]. Moreover, the surface atomic concentration of C in COO/COOH is significantly higher inside the wear track (i.e., 30.8 at. %) compared to outside the wear track (i.e., 20.2 at. %) (Fig. 6a and b) and for the surface lubricated with G_{aq} (i.e., 21.2 at. %, Fig. S4a). These results indicate that CGQDs were adsorbed onto the worn surface of the steel during the friction process.

The HR O 1s spectrum for the analysis spot inside and outside the wear track was deconvoluted into five peaks (Fig. 6c and d). The peak centred at 529.8 eV corresponds to iron oxide with a higher contribution outside the wear track, while the peak centred at an E_B of 530.9 eV corresponds to FeOOH [39]. The peak at 531.8 eV corresponds to COO/COOH [64], with a higher contribution inside the wear track than outside (Fig. 6c and d). In addition, the peak at 532.9 eV was attributed to C–OH [64,65], while the peak corresponding to water molecules

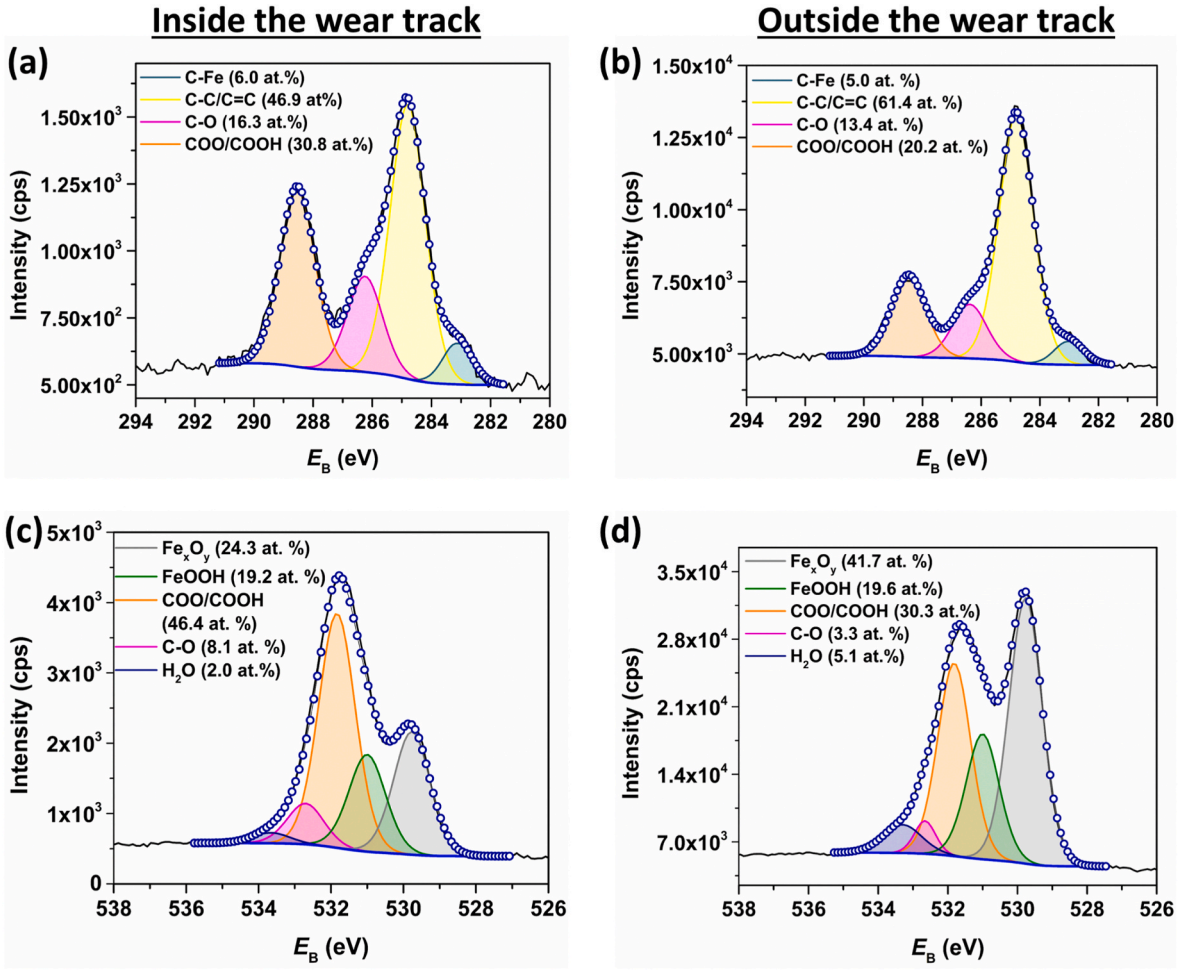

Fig. 6. High-resolution (HR) XPS spectra of C 1s and O 1s (a,c) inside the wear track and (b,d) outside the wear track, lubricated with 0.1 wt% $CGQDs_{aq}$ (test conditions: 3.5 N, 0.1 m/s). The diameter of the analysed spot size for the measurements inside the wear track was 55 μm.

indicates that they were either adsorbed from moist air or formed during the degradation of glycerol [23]. The corresponding high intensity of COO/COOH inside the wear track and the appearance of an additional C–Fe peak indicates that the CGQDs were adsorbed onto an oxidized steel surface that is exposed during the running-in period as a consequence of wear, as also suggested by Restuccia et al. and Marchetto et al. [66,67]. In addition, the negative zeta-potential of the CGQDs (−33.4 mV) suggests the interaction of negatively charged CGQDs with positively charged worn-surface sites (Fig. S5). Raman spectroscopy also confirmed the adsorbed film, demonstrating that the CGQDs were adsorbed on the worn surface.

On the other hand, the XPS measurements on the surface lubricated with G_{aq} (Fig. S4) showed that the surface atomic concentrations of C in C–OH (24.0 at. %) and O in FeOOH (32.8 at. %) were higher than that of the surface lubricated with $CGQDs_{aq}$. This indicates that the tribochemical reaction on the surface lubricated with $CGQDs_{aq}$ was less intense than the surface lubricated with G_{aq} [24], which in turn leads to less wear and shortens the running-in time, as observed for the wear analysis (Fig. 4a).

ToF-SIMS analysis was further performed to investigate the surface layer of the adsorbed tribofilm on the worn surface lubricated with 0.1 wt% $CGQDs_{aq}$. Fig. S6 shows the negative-ion and positive-ion ToF-SIMS spectra in the range 0–300 *m/z* and 0–150 *m/z*, respectively. The signals for $C_5H_9O_2^-$, $C_6H_5O_2^-$, $C_5H_3O_3^-$, $C_7H_5O_2^-$, $C_7H_6O_2^-$, $C_5H_5O_4^-$, $C_8H_5O_3^-$, $C_9H_{15}O_2^-$, $C_{10}H_{19}O_2^-$, $C_6H_5O_6^-$, $C_{12}H_{13}O_2^-$, $C_9H_3O_5^-$, $C_{12}H_{23}O_2^-$ in Fig. S6a might originate from the CGQDs. Moreover, Fig. S6b shows ToF-SIMS spectra in a positive polarity with various hydrocarbon related signals ($C_xH_y^+$). These signals can originate from the advantageous carbon species that adsorbed on the sample surface during sample handling, or they may result from the fragmentation of the CGQDs.

The signal at *m/z* 211.06 corresponds to $C_9H_{15}O_2Fe^-$ (Fig. S6a). In addition, Fig. S7 shows signals corresponding to CH_3OFe^+ at *m/z* 86.88 and $C_6H_5OFe^+$ at *m/z* 148.95, indicating the possible interaction of CGQDs with the worn surface.

Subsequently, the depth profiling associated with the 3D ToF-SIMS imaging was performed in a negative polarity to investigate the spatial distribution of COO^- and FeO_2^- in the tribolayer (Fig. 7). Fig. 7b shows that the topmost surface layer consists of species containing COO^- (which most likely mainly originates from the CGQDs). The FeO_2^- signal that comes from the iron oxide [68,69] was also present on the topmost layer despite the abundance of COO^-. Fig. 7b shows that by sputtering the sample with GCIB, in the deeper subsurface region (below the topmost position), is a mixed and inhomogeneous layer of iron oxide (characterized by the FeO_2^- signal) and COO^- species. These findings further suggest the adsorption of CGQDs on the worn surface.

3.4. Investigation of tribofilm

The microstructural, compositional, and bonding features of the tribofilm formed on the worn surface lubricated with 0.1 wt% $CGQDs_{aq}$ (3.5 N, 0.1 m/s) were characterized using the analytical techniques HRTEM and STEM, equipped with EDS and EELS, to gain a further insight into the underlying mechanism responsible for the superlubricity. Compared with traditional TEM, STEM is a much more powerful technique, offering advanced Z-contrast-imaging capabilities with atomic-level resolution [70]. The in-situ lift-out technique using the FIB-SEM dual system was used to prepare a thin cross-sectional lamella from the worn surface. The location of the FIB's cut position and the cross-sectional image of a few-nanometres thick lamella are shown in Fig. S8.

The BF-STEM image in Fig. 8a shows that a tribofilm with a thickness varying from 5 nm to 22 nm is formed during the friction test, which can be clearly seen between the dense Cr layer and the steel substrate. Interestingly, the image of the tribofilm at higher magnification shows the presence of a uniform sublayer of iron oxide of about 2.2 nm between the interface of the carbon-rich tribofilm and the steel substrate (Fig. 8b). The EDS elemental mapping and line scanning across the tribofilm show the high oxygen concentration in the grey layer, confirming the formation of the iron oxide layer (Fig. 8e). The formation of an iron oxide layer indicates the tribo-oxidation of the friction pairs, which occurs due to the more frequent direct contact during the initial running-in phase of the friction test. This iron oxide layer is covered with a tribofilm derived from the CGQDs, which is a chemically adsorbed layer formed by the symmetrical carboxylayte binding onto the iron oxide surface in the presence of an aqueous lubricant [71]. This indicates the passivation effect provided by the CGQDs [66,67], which reduces the wear by reducing the severity of the tribochemical reaction and provides a low-shearing interface for the realization of superlubricity. Moreover, Fig. 8b shows that the CGQDs are highly deformed and could not maintain their original morphology (compared to the original CGQDs) under the influence of a high contact pressure and continuous sliding. The splitting of the D and G bands and the increase of the I_D/I_G ratio observed in the Raman analysis of the worn surface further support the structural deformation of the CGQDs (Fig. 5).

The BF-STEM image of the tribofilm reveals the presence of an ordered graphitic layer along the sliding interface (Fig. 8c), implying that the interface is likely to transform from steel/steel to graphite/graphite-like interface. This observation is also confirmed by the appearance of a

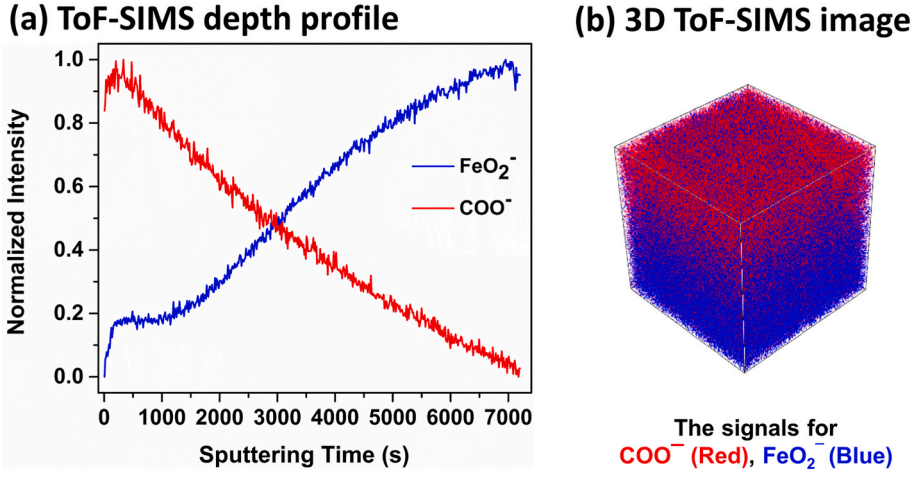

Fig. 7. (a) ToF-SIMS depth profile and (b) 3D ToF-SIMS image obtained in a negative polarity for COO^- and FeO_2^-. GCIB sputtering was performed using 5.0-keV Ar_{1900}^+ on an area of 500 × 500 μm, while the analysis was performed on an area of 300 × 300 μm. The height of these images in the z direction is not proportional to the scale in the x and y directions.

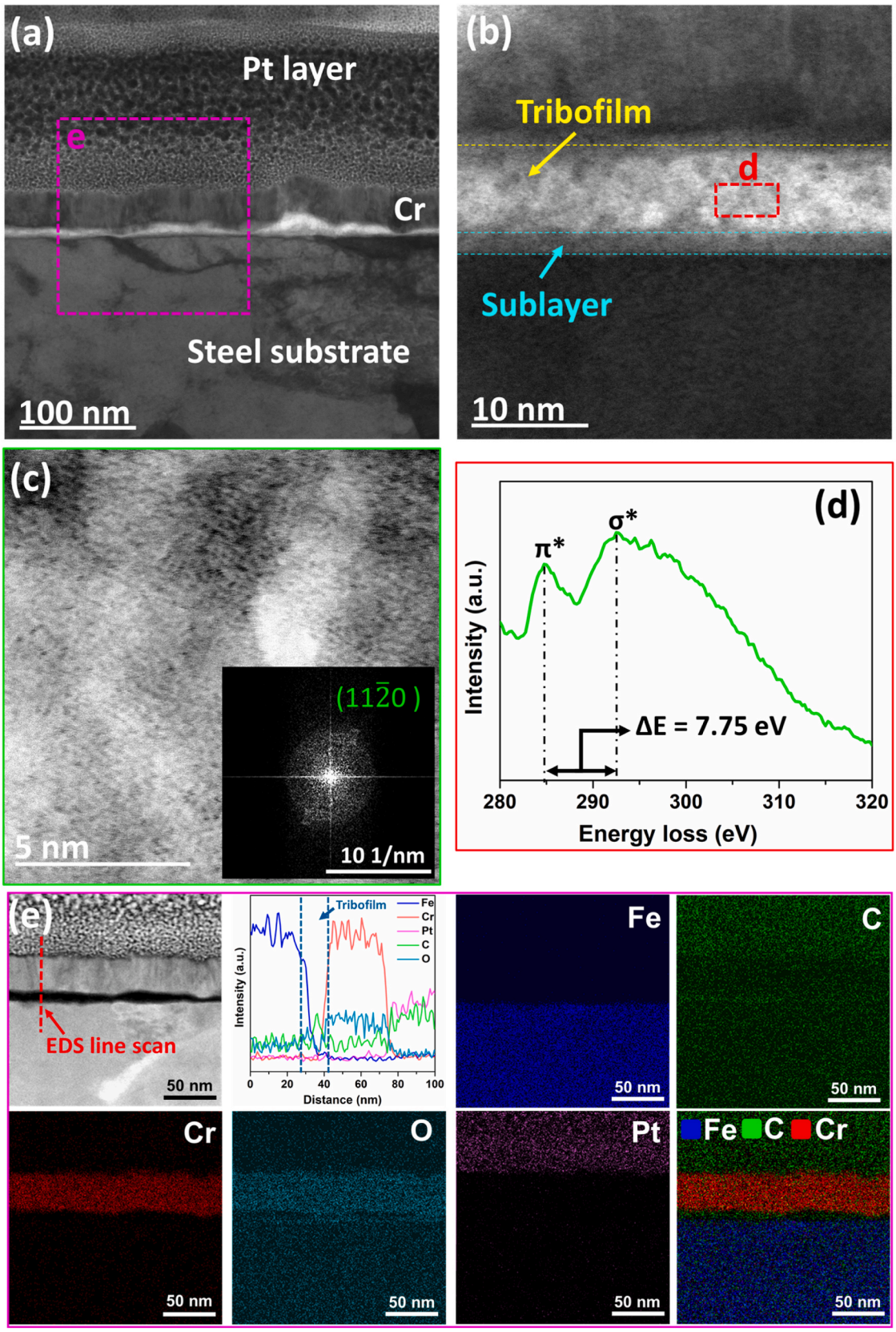

Fig. 8. STEM cross-sectional investigation of the tribofilm formed on the worn steel surface lubricated with 0.1 wt% $CGQDs_{aq}$ (3.5 N, 0.1 m/s). (a–b) BF-STEM image of the lamella cross-section indicating a tribofilm between the dense Cr layer and the steel substrate, (c) BF-STEM image of the tribofilm indicating a layered graphitic structure across the sliding direction (inset is a FFT of the crystalline feature, corresponding to a 11 $\bar{2}$ 0 graphitic plane), (d) EELS spectrum of the C–K edge obtained inside the tribofilm in an area marked with "d" in Fig. 8b showing the presence of sp^2-bonded carbon inside the tribofilm, (e) EDS elemental mapping and line-scan analysis across the tribofilm cross-section of the selected area marked with "e" in Fig. 8a.

sharp 2D band in the Raman spectrum of the worn surface, demonstrating the presence of a multilayer graphitic structure (Fig. 8c) [61]. The fast Fourier transform (FFT) analysis of Fig. 8c indicates that the crystalline feature corresponds to the lattice fringes of the 11 $\bar{2}$ 0 graphitic plane, possessing a lattice spacing of ~0.24 nm [47]. This suggests that the sliding-induced structural transformation of the CGQDs into the layered structure is one of the main reasons for the realization of superlubricity. To better illustrate the characteristics and bonding structure of the carbon in the tribofilm, the EELS core-edge spectrum of the C–K edge was recorded in the region marked in Fig. 8b. The C–K edge spectrum in Fig. 8d exhibits a well-defined line at 284.75 eV corresponding to the 1s→π*, and broad line at around 292.5 eV corresponding to the 1s→σ* transition of the sp^2 hybridized carbon at the K-edge region. The energy difference between the π* and σ* is 7.75 eV, as also found by Tang et al. for the GQDs [72]. The occurrence of the π* confirms the presence of sp^2-bonded carbon inside the tribofilm. The EDS elemental mapping and line-scan analysis across the cross-section of the tribofilm indicate that the tribofilm is enriched in C, which is confirmed by the superimposed mapping of Fe, C, and Cr presented in Fig. 8e. These results suggest that the formation of an iron oxide sublayer and the CGQDs-based tribolayer are key factors for the superlubricity.

3.5. Robustness and longevity of superlubricity

An additional series of start-stop friction tests were performed after the running-in phase, to comprehensively assess the role of the lubricating film and the robustness of the superlubricity under various speeds and loading conditions (Fig. 9). Initially, the test was performed at a sliding speed of 0.1 m/s and a normal applied load of 3.5 N, using a 50-μL droplet of $CGQDs_{aq}$ (stage i). The superlubricity state (μ < 0.01) was achieved after just 55 m of sliding distance. Then, after 20 min of sliding, the test was halted without altering the horizontal positions of the friction pairs. The test was again started (step ii) after a gap of 30 min, without removing the lubricant residue or cleaning the tribo-pairs. The aim was to evaluate the influence of contamination on the superlubricity performance. It can be seen that the COF remains in the superlubricity range, where the COF is about 0.007, indicating the facile recovery of the superlubricity during the in-situ friction test.

Subsequently, a series of start-stop tests were performed by varying the sliding speeds from 0.05 to 0.15 m/s (steps iii to v), then lowered back to 0.04 m/s (step vi). This observation revealed that the COF fluctuated slightly during the start-stop period; nevertheless, it remained in the superlubricity range.

Afterwards, the test was stopped and resumed at a sliding speed of 0.05 m/s by increasing the load from 3.5 to 5 N (step vii). Remarkably, the superlubricity state (μ < 0.01) was attained after just 100 s of running-in time. Subsequently, when the applied load increased to 10 N (step vii), the initial COF in the running-in phase was about 0.045, which was considerably lower than that in the initial step (i.e., step i). This improvement can be attributed to the already-adsorbed and exfoliated CGQDs on the sliding interface from the preceding steps. The COF reached less than 0.01 after a sliding distance of just 26 m (about 52 % shorter than in step i) and continued to decrease, eventually reaching a steady-state COF of 0.006 after about 43 m of sliding. Compared to step vii, this slightly longer running-in phase is due to the increased contact pressures with an increasing applied load, which causes inevitable wear of the contact pairs due to the increased direct contact between the surface asperities. Nevertheless, thanks to the rapid and robust adsorption ability of the carboxylates groups present on the CGQD surfaces, which ultimately leads to the regeneration of the lubricating film responsible for the superlubricity.

Next, the contact pairs were thoroughly cleaned with ethanol and water to remove the tribofilm or any residual lubricant from the surface, while maintaining the horizontal position of the tribo-pair unchanged. Afterwards, an in-situ friction test was initiated with a freshly added droplet of $CGQDs_{aq}$ (step ix, Fig. 9). In contrast to the swift restoration of the superlubricity observed in the preceding experiments, a running-in process with a gradually decreasing COF was observed before achieving the superlubricity state. However, the superlubricity was achieved after a sliding of 14 m, which is less than steps i and vii, respectively. These findings suggest that the formation of a tribofilm derived from CGQDs emerges as a crucial factor in achieving superlubricity. In the final stage (step x), both surfaces were thoroughly cleaned to remove the residual lubricant and tribofilm from the surface and then made to slide again with the addition of a water droplet. The COF immediately increased sharply and reached about 0.3, resembling the same frictional behaviour as observed in Fig. 2a for pure water.

Fig. 9 shows that the superlubricity sustained various sliding conditions, which is a notable achievement; however, maintaining consistently ultra-low friction below 0.01 for a longer duration is challenging [73,74]. Therefore, to ascertain the longevity of the superlubricity,

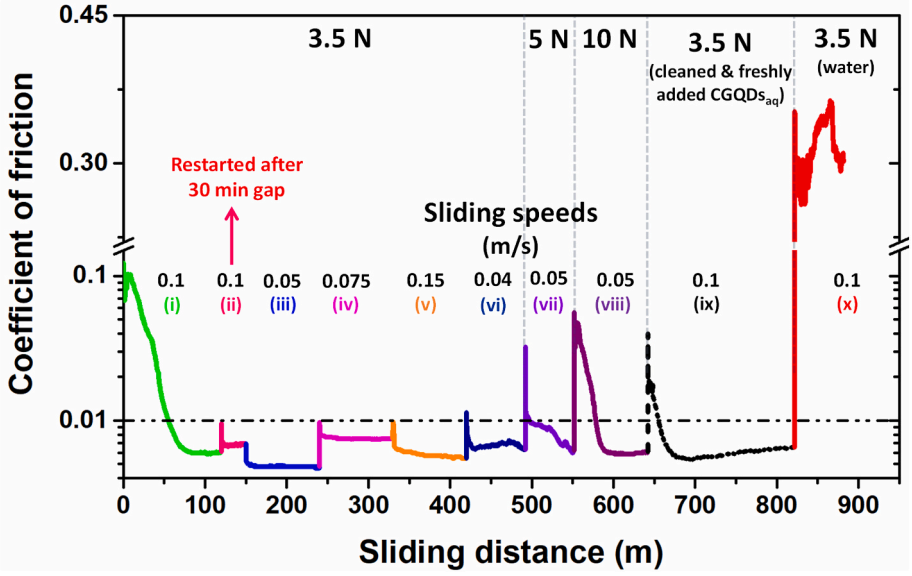

Fig. 9. Evaluation of the robustness and stability of the superlubricity by performing in-situ start-stop tests under various sliding speeds and loading conditions. The tests were performed without altering the horizontal position of the friction pairs using 0.1 wt% $CGQDs_{aq}$. Step x was performed using pure water.

prolonged intermittent friction tests were performed for a total sliding distance of 10,800 m (~13 X longer than in Fig. 9) using a 50 μL droplet of $CGQDs_{aq}$ (Fig. 10). Initially, the test was performed for a longer duration of 10 h (3.6 km sliding), and the results showed that superlubricity remained stable throughout the test. The test was then stopped, and the samples were unloaded and separated for a 4-h interval, during which the horizontal position of the friction pairs remained unchanged, and no additional lubricant was introduced. Afterwards, the test was restarted for another 15 h (5.4 km sliding) and the $CGQDs_{aq}$ maintained its superlubricity performance, and the COF remained unchanged after the pause. Then, the test was started again for 5 h (1.8 km sliding), and the COF stayed in the same superlubricity regime below 0.01. After prolonged sliding, Raman spectra were acquired on the worn surfaces, as shown in Fig. S9. The observance of characteristic D, G, and higher-order 2D bands corresponds to the graphitic carbon structure [61], implying that the graphite-based tribofilm derived from CGQDs remains adsorbed onto the contact surfaces even after prolonged sliding. This shows that once the tribofilm derived from CGQDs is formed, it continues to provide superlubricity for an extended period of sliding, and different contact condition variations do not harm it either.

These observations demonstrate that the formed lubricating film remained stable in its natural state under ambient conditions, which is critical in industrial applications where start-stop operations can cause severe damage and shorten equipment's service life due to COF fluctuations.

4. Discussion

Our findings show that CGQDs nano-additives in aqueous glycerol can provide superlubricity under various tribological parameters and enhance the load-bearing capacity in boundary lubrication compared to previously reported studies on aqueous lubricants [16–19,27,28]. However, the applicability of superlubricity for practical engineering applications depends on several factors, such as the stability of the lubricant, the ability to provide superlubricity at a high contact pressure in boundary lubrication, and the formation of a stable and robust tribofilm that is not affected by the variation of tribological parameters and start-stop conditions [75–77]. These factors are discussed in the following sections.

4.1. Stability of CGQD-based nano-lubricant

The stability of nanoparticles is one of the primary prerequisites for their use as lubricant additives. Fig. 1f shows the dispersion stability of $CGQDs_{aq}$ by irradiating the lubricant under a UV lamp. The consistent and uniform emission of the blue colour from the lubricant shows that the CGQDs remain stable and uniform without aggregating, even after 6 months of preparation. In addition, prolonged friction with old $CGQDs_{aq}$ (standing for 6 months after preparation) shows that it retains its lubrication performance and provides superlubricity (Fig. S3a). This excellent compatibility of CGQDs with aqueous glycerol is due to their ultra-small size, high surface-to-volume ratio, and the polar groups (i.e., - OH and –COOH) on their surface, as shown in Fig. 1d.

4.2. Contact pressure during the superlubricity state

The problem with steel/steel contacts lubricated with aqueous or water-based lubricants is that the superlubricity is observed almost exclusively in a mixed-lubrication regime, or the FCP is low during the superlubricity state [16–19,27,28]. This low FCP is either due to a rigorous tribochemical reaction or the inevitable wear of tribo-pairs during the running-in period, which causes the transition from boundary-to a mixed-lubrication regime. Furthermore, most of the studies based on the superlubricity between the self-mated steel contact involve uni-directional motion [16,18,19], contrary to the reciprocating motion, which is even more severe due to the zero velocity at the end of the stroke, and where it is hard to maintain the lubricating film to realize superlubricity [78]. Therefore, protecting the surface from wear and reducing friction in the boundary-lubrication regime is a major requirement for most industrial applications [75]. We observed that the CGQDs exhibit excellent lubrication properties and provide superlubricity in the boundary-lubrication regime at a contact pressure as high as 123 MPa, which is almost five times higher than existing findings relating to superlubricity in boundary lubrication employing an aqueous lubricant (Fig. 11). This higher contact pressure is attributed to the tribofilm formed by the CGQDs, which improve the load-bearing capacity

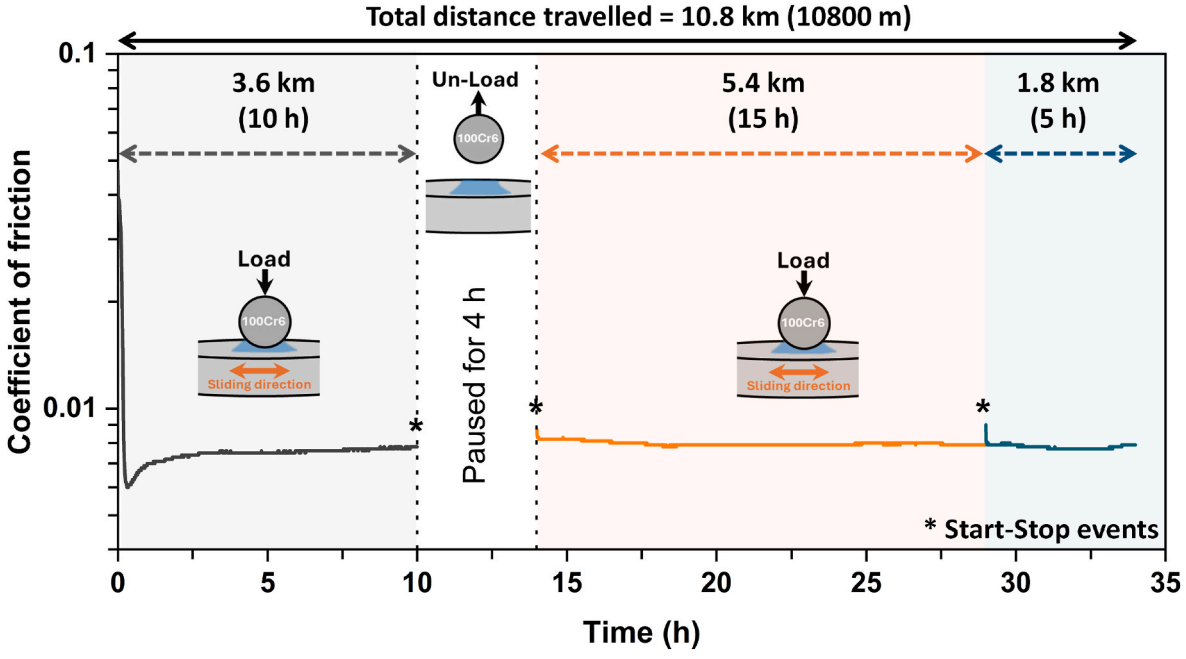

Fig. 10. Prolonged friction tests demonstrating the longevity of the superlubricity. The tests were performed using a 50 μL droplet of 0.1 wt% $CGQDs_{aq}$ without changing the horizontal position of the friction pairs; the applied load was 3.5 N, and the sliding speed was 0.1 m/s.

and mitigate the surface wear during the running-in period.

4.3. Significance of robustness and stability of superlubricity

Macroscale superlubricity is rarely observed in steel/steel contacts and is very sensitive to tribological parameters and specific environmental conditions, such as sliding speed, contact pressure, humidity, temperature, and type of lubricant. Slight variations in these conditions can disrupt the sensitive lubricating film, leading to an increase in friction. Another concern is that contaminants can disrupt the superlubricity behaviour, and even a minute quantity of impurity or particles can affect the lubricating film, leading to a loss of superlubricity performance [77]. Consequently, maintaining superlubricity over a prolonged duration and across diverse operating conditions is imperative for practical applications [75–77]. Our observations shown in Fig. 9 indicate that alterations in the system state, such as sliding speeds and the introduction of a new contact pressure, do not significantly affect the superlubricity during the start-stop period, and the formed lubricating film remained stable in its natural state under ambient conditions. Moreover, once a tribofilm derived from CGQDs is formed, it continues to provide superlubricity for an extended period (Fig. 10). This outcome is important, as the substantial fluctuations in the COF during the starting and stopping of industrial production equipment can lead to severe damage and impact the overall service life of the equipment.

4.4. Proposed mechanism for the macroscale superlubricity

A determination of the lubrication regime is crucial to elucidate the underlying superlubricity mechanism of the $CGQDs_{aq}$ between the self-mated steel surfaces. Therefore, to ascertain the lubrication regime during the superlubricity period, a minimum lubricating film thickness was estimated using the Hamrock–Dowson equation [79]. Finally, the ratio of the calculated film thickness to the combined surface roughness of the worn tribo-pairs (λ) was used to classify the lubrication regime [79]. Detailed information about the calculation process can be found in the supporting information (see NOTE S2). The calculated central film thickness with 0.1 wt% $CGQDs_{aq}$ (based on Table S4) ranged from 19.9 to 24.1 nm (i.e., 23.0 nm for 2 N, 19.9 nm for 3.5 N, 22.4 nm for 5 N, and 24.1 nm for 10 N). In contrast, it was 33.6 nm when lubricated with G_{aq}, almost 44 % more than the surface lubricated with $CGQDs_{aq}$. The lower film thickness in the case of $CGQDs_{aq}$ is primarily due to the higher contact pressure in the superlubricity condition resulting from a smaller WSD (123 MPa compared to 58 MPa for G_{aq} lubrication). In addition, the λ-value for $CGQDs_{aq}$ was found to be in the range 0.82–0.93, implying that the superlubricity was primarily observed in the boundary-lubrication regime [80]. These results indicate that the observed superlubricity is not due to a change in the lubrication regime, but is due to boundary-lubrication mechanisms such as the ball-bearing effect, the mending effect, and the formation of a boundary lubricating film between tribo-pairs [24,31–33].

Therefore, based on the above analysis and our findings, the primary lubrication mechanism for the superlubricity is proposed and illustrated in Fig. 12. During the running-in process, the COF drastically reduced to the superlubricity range within ~620 s (3.5 N, 0.1 m/s), indicating that the physical and the chemical structures of the CGQDs play a dominant role in friction reduction, and at the same time protect the surface from excessive wear under extreme boundary conditions. Firstly, the super-small size (i.e., ~2.6 nm) and excellent stability of the CGQDs in aqueous glycerol ensure the continuous supply of CGQDs between the rubbing surfaces, which facilitates the formation of a solid-lubrication film during asperity contact under the influence of pressure, resulting in a lowering of the friction and wear to some extent. Secondly, it is well-accepted that during the running-in phase, the steel surface becomes positively charged due to the release of low-energy electrons, resulting in exposure of Fe^{2+} and Fe^{3+} on the rubbing surfaces [31,35,81]. Therefore, during the early stages of the running-in period, the carboxylic anions on the surface of the CGQDs facilitate their adsorption by binding strongly with the preferentially exposed iron cations on the worn surface [36,38], which protects the surface from excessive wear by mitigating the direct asperity contact (Fig. 12a). In addition, due to the large surface area of the CGQDs, they have numerous active moieties to react with the worn steel surface under the influence of a high contact pressure and the frictional heat, expediting the formation of a boundary tribo-chemical film. The XPS and ToF-SIMS analyses of the worn surface further support the adsorption of CGQDs (Figs. 6 and 7). Thirdly, the worn surfaces are relatively smooth and polished without noticeable abrasive marks compared to the surfaces lubricated with G_{aq} (Fig. 4a), indicating a positive nano-lubrication effect provided by the CGQDs. Nevertheless, this polishing effect could also be due to increased C–OH groups on the worn surface (Fig. 6a), which could act as low-friction brushes while preventing the asperity contact [23,82,83] and promote chemical polishing in an aqueous lubricating environment, as suggested by Long et al. [23,84]. This indicates the positive lubrication effect of the synergistic role played by the tribofilm derived from the CGQDs and

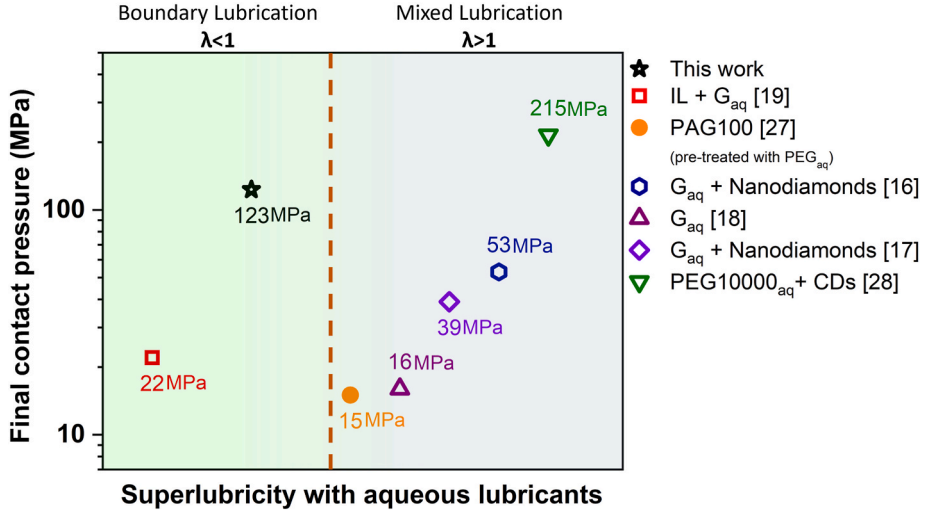

Fig. 11. Comparison of the final contact pressure (FCP) during the superlubricity state of this study and other self-mated steel systems lubricated with aqueous lubricants [16–19,27,28]. The FCP is calculated by dividing the normal applied load by the contact area of the worn region on the ball. (Note that this comparison graph is for pin-on-disk systems only)

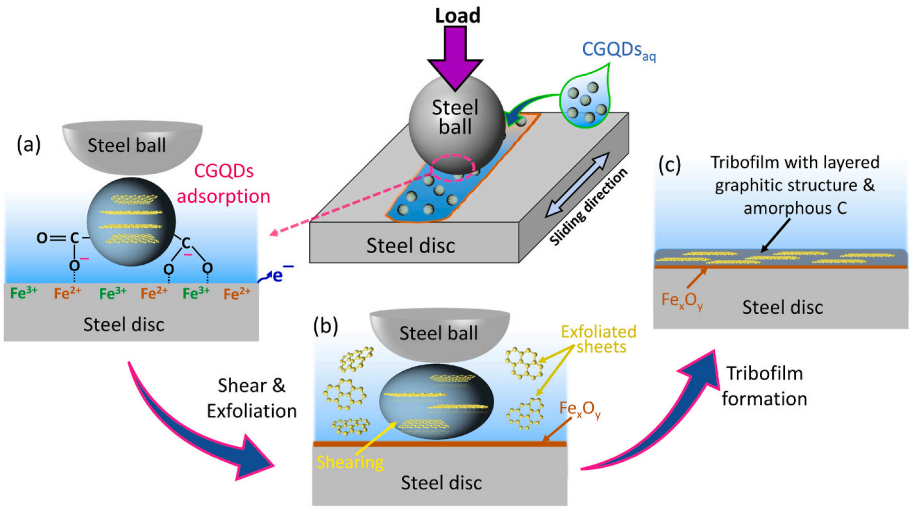

Fig. 12. Schematic of the proposed superlubricity mechanism of CGQDs$_{aq}$ in a steel/steel contact. (a) Adsorption of CGQDs on the worn steel surface; (b) tribo-induced shearing and exfoliation of graphene sheets inside CGQDs; (c) tribofilm with structurally transformed CGQDs to layered graphitic structure.

aqueous glycerol with dispersed CGQDs. Lastly, due to the continuous inter-layer shearing and exfoliation of the graphene sheets within the CGQDs (Fig. 12b), the adsorbed CGQDs on the tribo-oxidized worn surface underwent a sliding-induced structural transformation to the layered graphitic structure, which is mainly responsible for the superlubricity being achieved (Fig. 12c). This implies that the structure of the CGQDs plays a pivotal role in achieving superlubricity. The importance of the CGQD structure was further testified by performing the friction test between self-mated a-C:H (Fig. 2b), which is regarded as a non-reactive surface and provides high friction in humid and aqueous environments [85]. The COF decreased to 0.015 after a long running-in period. This decrease in friction could be attributed to a physical mechanism that relies on the shearing of the graphene layers within the CGQDs, suggesting that the structure of the CGQDs plays a role in reducing the friction. However, the interlayer shearing of the graphene is not solely responsible for the superlubricity in steel tribo-pairs; the adsorption of the CGQDs to the metallic surface via tribochemical reaction is a prerequisite for forming a super-lubricious layer.

The above findings suggest that the chemically adsorbed film containing structurally transformed CGQDs passivates the tribo-oxidized surface and protects it from excessive wear and oxidation during the running-in process [6], consequently leading to a higher contact pressure during superlubricity in the boundary-lubrication regime, compared to available studies based on aqueous lubricants [16,18,19,27,39]. Therefore, this excellent lubrication effect is due to the synergistic adsorption, shearing and polishing effect provided by the CGQDs dispersed in aqueous glycerol. In particular, the chemical adsorption of CGQDs onto the worn surface protects the tribo-pairs from excessive wear. At the same time, the structural transformation of the CGQDs to the graphitic layered structure due to continuous exfoliation and shearing of the graphene structure inside the CGQDs resulted in the realization of superlubricity. This research not only sheds light on the active lubrication mechanism for superlubricity between the steel contacts, but it also clarifies the role of the CGQDs' physical and chemical structure in achieving superlubricity. As a result, we believe this study is a significant step forward in the pursuit of superlubricity in steel contacts operating under aqueous lubrication conditions, especially at high contact pressures, thereby establishing a foundation for their practical applicability in mechanical systems.

5. Conclusion

CGQDs as an additive in aqueous glycerol provide robust superlubricity between self-mated steel contacts for various tribological parameters with a COF between 0.005 and 0.0095, which is a 72–78 % reduction in friction compared to aqueous glycerol without any nano-additives. At the same time, surface wear is greatly suppressed, resulting in a final contact pressure during the superlubricity state as high as 123 MPa, which elevates the upper limit of contact pressure under boundary-lubrication conditions in aqueous lubricated steel contacts. This enhancement in lubrication performance is ascribed to the robust adsorption ability of CGQDs on the worn surface, combined with the sliding-induced structural degradation and transformation of CGQDs into a layered graphitic structure, which led to the generation of a low-shear interface. Once a tribofilm with structurally transformed CGQDs is formed, it can maintain its superlubricity state and adapt to different sliding conditions without an additional supply of CGQDs$_{aq}$. This study is a major advance in the search for superlubricity in steel contacts because we were able to clarify the role of chemical adsorption and the structural transformation of CGQDs in achieving superlubricity under aqueous lubricated conditions.

CRediT authorship contribution statement

Irfan Nadeem: Writing – review & editing, Writing – original draft, Methodology, Investigation, Formal analysis, Data curation. **Matjaž Finšgar:** Writing – review & editing, Validation, Investigation, Formal analysis, Data curation. **Goran Dražić:** Writing – review & editing, Validation, Software, Investigation, Formal analysis, Data curation. **Matjaž Malok:** Data curation. **Ardian Morina:** Writing – review & editing, Visualization. **Mitjan Kalin:** Writing – review & editing, Visualization, Supervision, Resources, Methodology, Funding acquisition, Conceptualization.

Declaration of competing interest

The authors declare that they have no known competing financial interests or personal relationships that could have appeared to influence the work reported in this paper.

Acknowledgment

This research is financially supported by the European Union's Horizon 2020 research and innovation program under the Marie Skłodowska-Curie Action, Grant Agreement no. 860246. The authors also acknowledge financial support from the Slovenian Research and Innovation Agency (ARIS), core fundings no. P2-0231, P2-0421, P2-0118, PR-11224 and P1-0099. The authors also like to acknowledge the

support from the Nanocenter, Ljubljana, Slovenia, for providing the FIB-SEM dual system. The author Matjaž Finšgar would like to acknowledge the co-financial support by the Republic of Slovenia, the Ministry of Higher Education, Science and Innovation, and the European Union through the European Regional Development Fund.

Appendix A. Supplementary data

Supplementary data to this article can be found online at https://doi.org/10.1016/j.carbon.2024.119226.

References

[1] K. Holmberg, A. Erdemir, The impact of tribology on energy use and CO2 emission globally and in combustion engine and electric cars, Tribol. Int. 135 (2019) 389–396, https://doi.org/10.1016/j.triboint.2019.03.024.
[2] E. Ciulli, Tribology and sustainable development Goals, in: G. Quaglia, A. Gasparetto, V. Petuya, G. Carbone (Eds.), Proceedings of I4SDG Workshop 2021, Springer International Publishing, Cham, 2022, pp. 438–447, https://doi.org/10.1007/978-3-030-87383-7_48.
[3] J. Luo, M. Liu, L. Ma, Origin of friction and the new frictionless technology—superlubricity: Advancements and future outlook, Nano Energy 86 (2021) 106092, https://doi.org/10.1016/j.nanoen.2021.106092.
[4] D. Berman, A. Erdemir, A.V. Sumant, Approaches for achieving superlubricity in two-dimensional materials, ACS Nano 12 (2018) 2122–2137, https://doi.org/10.1021/acsnano.7b09046.
[5] M.Z. Baykara, M.R. Vazirisereshk, A. Martini, Emerging superlubricity: a review of the state of the art and perspectives on future research, Appl. Phys. Rev. 5 (2018) 041102, https://doi.org/10.1063/1.5051445.
[6] Y. Liu, X. Ge, J. Li, Graphene lubrication, Appl. Mater. Today 20 (2020) 100662, https://doi.org/10.1016/j.apmt.2020.100662.
[7] H. Li, J. Wang, S. Gao, Q. Chen, L. Peng, K. Liu, X. Wei, Superlubricity between MoS2 monolayers, Adv. Mater. 29 (2017) 1701474, https://doi.org/10.1002/adma.201701474.
[8] Y. Liu, J. Li, J. Li, S. Yi, X. Ge, X. Zhang, J. Luo, Shear-induced interfacial structural conversion triggers macroscale superlubricity: from black phosphorus nanoflakes to phosphorus oxide, ACS Appl. Mater. Interfaces 13 (2021) 31947–31956, https://doi.org/10.1021/acsami.1c04664.
[9] X. Feng, S. Kwon, J.Y. Park, M. Salmeron, Superlubric sliding of graphene nanoflakes on graphene, ACS Nano 7 (2013) 1718–1724, https://doi.org/10.1021/nn305722d.
[10] X. Ge, Z. Chai, Q. Shi, Y. Liu, W. Wang, Graphene superlubricity: a review, Friction 11 (2023) 1953–1973, https://doi.org/10.1007/s40544-022-0681-y.
[11] R. Zhang, Z. Ning, Y. Zhang, Q. Zheng, Q. Chen, H. Xie, Q. Zhang, W. Qian, F. Wei, Superlubricity in centimetres-long double-walled carbon nanotubes under ambient conditions, Nat. Nanotechnol. 8 (2013) 912–916, https://doi.org/10.1038/nnano.2013.217.
[12] S. Kawai, A. Benassi, E. Gnecco, H. Söde, R. Pawlak, X. Feng, K. Müllen, D. Passerone, C.A. Pignedoli, P. Ruffieux, R. Fasel, E. Meyer, Superlubricity of graphene nanoribbons on gold surfaces, Science 351 (2016) 957–961, https://doi.org/10.1126/science.aad3569.
[13] S.-W. Liu, H.-P. Wang, Q. Xu, T.-B. Ma, G. Yu, C. Zhang, D. Geng, Z. Yu, S. Zhang, W. Wang, Y.-Z. Hu, H. Wang, J. Luo, Robust microscale superlubricity under high contact pressure enabled by graphene-coated microsphere, Nat. Commun. 8 (2017) 14029, https://doi.org/10.1038/ncomms14029.
[14] X. Ren, X. Yang, G. Xie, F. He, R. Wang, C. Zhang, D. Guo, J. Luo, Superlubricity under ultrahigh contact pressure enabled by partially oxidized black phosphorus nanosheets, Nat. Prod. J. Mater. Appl. 5 (2021) 1–12, https://doi.org/10.1038/s41699-021-00225-0.
[15] G. Tang, Z. Wu, F. Su, H. Wang, X. Xu, Q. Li, G. Ma, P.K. Chu, Macroscale superlubricity on engineering steel in the presence of black phosphorus, Nano Lett. 21 (2021) 5308–5315, https://doi.org/10.1021/acs.nanolett.1c01437.
[16] Z. Chen, Y. Liu, J. Luo, Superlubricity of nanodiamonds glycerol colloidal solution between steel surfaces, Colloids Surf. A Physicochem. Eng. Asp. 489 (2016) 400–406, https://doi.org/10.1016/j.colsurfa.2015.10.062.
[17] A.M. Tortora, D. Halenahally Veeregowda, Effects of two sliding motions on the superlubricity and wear of self-mated bearing steel lubricated by aqueous glycerol with and without nanodiamonds, Wear 386–387 (2017) 173–178, https://doi.org/10.1016/j.wear.2017.06.015.
[18] Z. Chen, Y. Liu, S. Zhang, J. Luo, Controllable superlubricity of glycerol solution via environment humidity, Langmuir 29 (2013) 11924–11930, https://doi.org/10.1021/la402422h.
[19] J. Hua, M. Björling, R. Larsson, Y. Shi, Controllable superlubricity achieved with mixtures of green ionic liquid and glycerol aqueous solution via humidity, J. Mol. Liq. 345 (2022) 117860, https://doi.org/10.1016/j.molliq.2021.117860.
[20] W. Ma, Z. Gong, K. Gao, L. Qiang, J. Zhang, S. Yu, Superlubricity achieved by carbon quantum dots in ionic liquid, Mater. Lett. 195 (2017) 220–223, https://doi.org/10.1016/j.matlet.2017.02.135.
[21] X. Ge, J. Li, H. Wang, C. Zhang, Y. Liu, J. Luo, Macroscale superlubricity under extreme pressure enabled by the combination of graphene-oxide nanosheets with ionic liquid, Carbon 151 (2019) 76–83, https://doi.org/10.1016/j.carbon.2019.05.070.
[22] X. Ge, J. Li, R. Luo, C. Zhang, J. Luo, Macroscale superlubricity enabled by the synergy effect of graphene-oxide nanoflakes and ethanediol, ACS Appl. Mater. Interfaces 10 (2018) 40863–40870, https://doi.org/10.1021/acsami.8b14791.
[23] Y. Long, M.-I.D.B. Bouchet, T. Lubrecht, T. Onodera, J.M. Martin, Superlubricity of glycerol by self-sustained chemical polishing, Sci. Rep. 9 (2019) 6286, https://doi.org/10.1038/s41598-019-42730-9.
[24] Y. Liu, S. Yu, J. Li, X. Ge, Z. Zhao, W. Wang, Quantum dots of graphene oxide as nano-additives trigger macroscale superlubricity with an extremely short running-in period, Mater. Nano Today 18 (2022) 100219, https://doi.org/10.1016/j.mtnano.2022.100219.
[25] M. Kano, J.M. Martin, K. Yoshida, M.I. De Barros Bouchet, Super-low friction of ta-C coating in presence of oleic acid, Friction 2 (2014) 156–163, https://doi.org/10.1007/s40544-014-0047-1.
[26] C. Matta, L. Joly-Pottuz, M.I. De Barros Bouchet, J.M. Martin, M. Kano, Q. Zhang, W.A. Goddard, Superlubricity and tribochemistry of polyhydric alcohols, Phys. Rev. B 78 (2008) 085436, https://doi.org/10.1103/PhysRevB.78.085436.
[27] X. Ge, T. Halmans, J. Li, J. Luo, Molecular behaviors in thin film lubrication—part three: superlubricity attained by polar and nonpolar molecules, Friction 7 (2019) 625–636, https://doi.org/10.1007/s40544-018-0254-2.
[28] C. Du, T. Yang, T. Yu, L. Zhang, X. Sui, Y. Feng, X. Wang, D. Wang, Accelerating Macroscale Superlubricity through Carbon Quantum Dots on Engineering Steel Surfaces, Adv. Funct. Mater. 34 (2024) 2310880. https://doi.org/10.1002/adfm.202310880.
[29] Y. Yan, J. Gong, J. Chen, Z. Zeng, W. Huang, K. Pu, J. Liu, P. Chen, Recent advances on graphene quantum dots: from chemistry and physics to applications, Adv. Mater. 31 (2019) 1808283, https://doi.org/10.1002/adma.201808283.
[30] P. Tian, L. Tang, K.S. Teng, S.P. Lau, Graphene quantum dots from chemistry to applications, Mater. Today Chem. 10 (2018) 221–258, https://doi.org/10.1016/j.mtchem.2018.09.007.
[31] Z. Mou, R. Yan, J. Peng, Y. Li, Z. Huang, Z. Wang, B. Zhao, D. Xiao, Synthesis of polyzwitterionic carbon dots with superior friction and fatigue control behaviors under water lubrication, Chem. Eng. J. 465 (2023) 142986, https://doi.org/10.1016/j.cej.2023.142986.
[32] I. Nadeem, M. Malok, J. Kovač, T. Bin Yaqub, A. Cavaleiro, M. Kalin, Superior macro-scale tribological performance of steel contacts based on graphene quantum dots in aqueous glycerol, Tribol. Int. 181 (2023) 108328, https://doi.org/10.1016/j.triboint.2023.108328.
[33] J. Tang, S. Chen, Y. Jia, Y. Ma, H. Xie, X. Quan, Q. Ding, Carbon dots as an additive for improving performance in water-based lubricants for amorphous carbon (a-C) coatings, Carbon 156 (2020) 272–281, https://doi.org/10.1016/j.carbon.2019.09.055.
[34] Y. Liu, S. Yu, Z. Fan, X. Ge, W. Wang, How does lateral size influence the tribological behaviors of graphene oxide as nanoadditive for water-based lubrication? Carbon 219 (2024) 118803 https://doi.org/10.1016/j.carbon.2024.118803.
[35] Z. Mou, B. Zhao, B. Wang, D. Xiao, Integration of functionalized polyelectrolytes onto carbon dots for synergistically improving the tribological properties of polyethylene glycol, ACS Appl. Mater. Interfaces 13 (2021) 8794–8807, https://doi.org/10.1021/acsami.0c22077.
[36] R. Simič, M. Kalin, Adsorption mechanisms for fatty acids on DLC and steel studied by AFM and tribological experiments, Appl. Surf. Sci. 283 (2013) 460–470, https://doi.org/10.1016/j.apsusc.2013.06.131.
[37] T. Kuwahara, P.A. Romero, S. Makowski, V. Weihnacht, G. Moras, M. Moseler, Mechano-chemical decomposition of organic friction modifiers with multiple reactive centres induces superlubricity of ta-C, Nat. Commun. 10 (2019) 151, https://doi.org/10.1038/s41467-018-08042-8.
[38] R.R. Sahoo, S.K. Biswas, Frictional response of fatty acids on steel, J. Colloid Interface Sci. 333 (2009) 707–718, https://doi.org/10.1016/j.jcis.2009.01.046.
[39] S. Sun, J. Li, J. Li, J. Luo, Enhanced superlubricity on a-C films by lubrication with 3-hydroxypropionic acid, Carbon 199 (2022) 161–169, https://doi.org/10.1016/j.carbon.2022.07.062.
[40] Y. Dong, J. Shao, C. Chen, H. Li, R. Wang, Y. Chi, X. Lin, G. Chen, Blue luminescent graphene quantum dots and graphene oxide prepared by tuning the carbonization degree of citric acid, Carbon 50 (2012) 4738–4743, https://doi.org/10.1016/j.carbon.2012.06.002.
[41] S. Kostromin, A. Borodina, A. Podshivalov, D. Pankin, O. Zhigalina, S. Bronnikov, Characterization of carbon quantum dots obtained through citric acid pyrolysis, Fullerenes, Nanotub. Carbon Nanostruct. 31 (2023) 931–939, https://doi.org/10.1080/1536383X.2023.2224467.
[42] L.B. Lane, Freezing points of glycerol and its aqueous solutions, Ind. Eng. Chem. 17 (1925) 924, https://doi.org/10.1021/ie50189a017, 924.
[43] J.A. Trejo González, M.P. Longinotti, H.R. Corti, The viscosity of Glycerol−Water mixtures including the supercooled region, J. Chem. Eng. Data 56 (2011) 1397, https://doi.org/10.1021/je101164q, 1406.
[44] J.L. Dashnau, N.V. Nucci, K.A. Sharp, J.M. Vanderkooi, Hydrogen bonding and the cryoprotective properties of glycerol/water mixtures, J. Phys. Chem. B 110 (2006) 13670–13677, https://doi.org/10.1021/jp0618680.
[45] M. Kalin, J. Kogovšek, M. Remškar, Nanoparticles as novel lubricating additives in a green, physically based lubrication technology for DLC coatings, Wear 303 (2013) 480–485, https://doi.org/10.1016/j.wear.2013.03.009.
[46] D. Berman, B. Narayanan, M.J. Cherukara, S.K.R.S. Sankaranarayanan, A. Erdemir, A. Zinovev, A.V. Sumant, Operando tribochemical formation of onion-like-carbon leads to macroscale superlubricity, Nat. Commun. 9 (2018) 1164, https://doi.org/10.1038/s41467-018-03549-6.
[47] A. Abbas, T.A. Tabish, S.J. Bull, T.M. Lim, A.N. Phan, High yield synthesis of graphene quantum dots from biomass waste as a highly selective probe for Fe3+

sensing, Sci. Rep. 10 (2020) 21262, https://doi.org/10.1038/s41598-020-78070-2.
[48] B. Lyu, H.-J. Li, F. Xue, L. Sai, B. Gui, D. Qian, X. Wang, J. Yang, Facile, gram-scale and eco-friendly synthesis of multi-color graphene quantum dots by thermal-driven advanced oxidation process, Chem. Eng. J. 388 (2020) 124285, https://doi.org/10.1016/j.cej.2020.124285.
[49] L. Li, G. Wu, G. Yang, J. Peng, J. Zhao, J.-J. Zhu, Focusing on luminescent graphene quantum dots: current status and future perspectives, Nanoscale 5 (2013) 4015–4039, https://doi.org/10.1039/C3NR33849E.
[50] M. Shehab, S. Ebrahim, M. Soliman, Graphene quantum dots prepared from glucose as optical sensor for glucose, J. Lumin. 184 (2017) 110–116, https://doi.org/10.1016/j.jlumin.2016.12.006.
[51] M. Muhyuddin, D. Testa, R. Lorenzi, G.M. Vanacore, F. Poli, F. Soavi, S. Specchia, W. Giurlani, M. Innocenti, L. Rosi, C. Santoro, Iron-based electrocatalysts derived from scrap tires for oxygen reduction reaction: Evolution of synthesis-structure-performance relationship in acidic, neutral and alkaline media, Electrochim. Acta 433 (2022) 141254, https://doi.org/10.1016/j.electacta.2022.141254.
[52] P. Zhao, M. Yang, W. Fan, X. Wang, F. Tang, C. Yang, X. Dou, S. Li, Y. Wang, Y. Cao, Facile one-pot conversion of petroleum asphaltene to high quality green fluorescent graphene quantum dots and their application in cell imaging, Part. Part. Syst. Char. 33 (2016) 635–644, https://doi.org/10.1002/ppsc.201600070.
[53] C.K. Chua, Z. Sofer, P. Šimek, O. Jankovský, K. Klímová, S. Bakardjieva, Š. Hrdličková Kučková, M. Pumera, Synthesis of strongly fluorescent graphene quantum dots by cage-opening buckminsterfullerene, ACS Nano 9 (2015) 2548–2555, https://doi.org/10.1021/nn505639q.
[54] N. Dhenadhayalan, K.-C. Lin, R. Suresh, P. Ramamurthy, Unravelling the multiple emissive states in citric-acid-derived carbon dots, J. Phys. Chem. C 120 (2016) 1252–1261, https://doi.org/10.1021/acs.jpcc.5b08516.
[55] S. Verma, R.K. Dutta, A facile method of synthesizing ammonia modified graphene oxide for efficient removal of uranyl ions from aqueous medium, RSC Adv. 5 (2015) 77192–77203, https://doi.org/10.1039/C5RA10555B.
[56] N.E. Lee, J.-M. Jeong, H.S. Lim, S.Y. Lee, S.O. Cho, Ultraviolet/blue light emitting high-quality graphene quantum dots and their biocompatibility, Carbon 170 (2020) 213–219, https://doi.org/10.1016/j.carbon.2020.08.015.
[57] S. Zhu, Y. Song, J. Wang, H. Wan, Y. Zhang, Y. Ning, B. Yang, Photoluminescence mechanism in graphene quantum dots: quantum confinement effect and surface/edge state, Nano Today 13 (2017) 10–14, https://doi.org/10.1016/j.nantod.2016.12.006.
[58] K. Fan, X. Chen, X. Wang, X. Liu, Y. Liu, W. Lai, X. Liu, Toward excellent tribological performance as oil-based lubricant additive: particular tribological behavior of fluorinated graphene, ACS Appl. Mater. Interfaces 10 (2018) 28828–28838, https://doi.org/10.1021/acsami.8b07635.
[59] M. Muhyuddin, E. Berretti, S.A. Mirshokraee, J. Orsilli, R. Lorenzi, L. Capozzoli, F. D'Acapito, E. Murphy, S. Guo, P. Atanassov, A. Lavacchi, C. Santoro, Formation of the active site structures during pyrolysis transformation of Fe-phthalocyanine into Fe-Nx-C electrocatalysts for the oxygen reduction reaction, Appl. Catal. B Environ. 343 (2024) 123515, https://doi.org/10.1016/j.apcatb.2023.123515.
[60] S. Bhowmick, A. Banerji, A.T. Alpas, Role of humidity in reducing sliding friction of multilayered graphene, Carbon 87 (2015) 374–384, https://doi.org/10.1016/j.carbon.2015.01.053.
[61] A.C. Ferrari, J.C. Meyer, V. Scardaci, C. Casiraghi, M. Lazzeri, F. Mauri, S. Piscanec, D. Jiang, K.S. Novoselov, S. Roth, A.K. Geim, Raman spectrum of graphene and graphene layers, Phys. Rev. Lett. 97 (2006) 187401, https://doi.org/10.1103/PhysRevLett.97.187401.
[62] K. Tripathi, G. Gyawali, S.W. Lee, Graphene coating via chemical vapor deposition for improving friction and wear of gray cast iron at interfaces, ACS Appl. Mater. Interfaces 9 (2017) 32336–32351, https://doi.org/10.1021/acsami.7b07922.
[63] S.J. Oh, D.C. Cook, H.E. Townsend, Characterization of iron oxides commonly formed as corrosion products on steel, Hyperfine Interact. 112 (1998) 59–66, https://doi.org/10.1023/A:1011076308501.
[64] R. Al-Gaashani, A. Najjar, Y. Zakaria, S. Mansour, M.A. Atieh, XPS and structural studies of high quality graphene oxide and reduced graphene oxide prepared by different chemical oxidation methods, Ceram. Int. 45 (2019) 14439–14448, https://doi.org/10.1016/j.ceramint.2019.04.165.
[65] S. Yi, X. Chen, J. Li, Y. Liu, S. Ding, J. Luo, Macroscale superlubricity of Si-doped diamond-like carbon film enabled by graphene oxide as additives, Carbon 176 (2021) 358–366, https://doi.org/10.1016/j.carbon.2021.01.147.
[66] P. Restuccia, M.C. Righi, Tribochemistry of graphene on iron and its possible role in lubrication of steel, Carbon 106 (2016) 118–124, https://doi.org/10.1016/j.carbon.2016.05.025.
[67] D. Marchetto, P. Restuccia, A. Ballestrazzi, M.C. Righi, A. Rota, S. Valeri, Surface passivation by graphene in the lubrication of iron: a comparison with bronze, Carbon 116 (2017) 375–380, https://doi.org/10.1016/j.carbon.2017.02.011.
[68] E. Gardin, S. Zanna, A. Seyeux, A. Allion-Maurer, P. Marcus, XPS and ToF-SIMS characterization of the surface oxides on lean duplex stainless steel – global and local approaches, Corrosion Sci. 155 (2019) 121–133, https://doi.org/10.1016/j.corsci.2019.04.039.
[69] L. Wang, A. Seyeux, P. Marcus, Thermal stability of the passive film formed on 316L stainless steel surface studied by ToF-SIMS, Corrosion Sci. 165 (2020) 108395, https://doi.org/10.1016/j.corsci.2019.108395.
[70] X. Chen, T. Kato, C. Zhang, J. Luo, Chapter 16 - tribo-induced interfacial nanostructures stimulating superlubricity in amorphous carbon films, in: A. Erdemir, J.M. Martin, J. Luo (Eds.), Superlubricity, second ed., Elsevier, 2021, pp. 289–307, https://doi.org/10.1016/B978-0-444-64313-1.00016-8.
[71] S. Yu, G.M. Chow, Carboxyl group (–CO2H) functionalized ferrimagnetic iron oxide nanoparticles for potential bio-applications, J. Mater. Chem. 14 (2004) 2781–2786, https://doi.org/10.1039/B404964K.
[72] L. Tang, R. Ji, X. Li, K.S. Teng, S.P. Lau, Size-dependent structural and optical characteristics of glucose-derived graphene quantum dots, Part. Part. Syst. Char. 30 (2013) 523–531, https://doi.org/10.1002/ppsc.201200131.
[73] C. Kumara, M.J. Lance, J. Qu, Macroscale superlubricity by a sacrificial carbon nanotube coating, Mater. Nano Today 21 (2023) 100297, https://doi.org/10.1016/j.mtnano.2022.100297.
[74] C. Du, T. Yu, L. Zhang, R. Shen, Z. Wu, X. Li, X. He, Y. Feng, D. Wang, Robust and universal macroscale superlubricity with natural phytic acid solutions, Tribol. Int. 183 (2023) 108387, https://doi.org/10.1016/j.triboint.2023.108387.
[75] W. Zhai, K. Zhou, Nanomaterials in superlubricity, Adv. Funct. Mater. 29 (2019) 1806395, https://doi.org/10.1002/adfm.201806395.
[76] O. Hod, E. Meyer, Q. Zheng, M. Urbakh, Structural superlubricity and ultralow friction across the length scales, Nature 563 (2018) 485–492, https://doi.org/10.1038/s41586-018-0704-z.
[77] M. Ramezani, Z.M. Ripin, C.-P. Jiang, T. Pasang, Superlubricity of materials: progress, potential, and challenges, Materials 16 (2023) 5145, https://doi.org/10.3390/ma16145145.
[78] Y. Liu, H. Zhang, Roles of transfer layer and surface adhesion on superlubricity behaviors of diamond-like carbon film depending on rotating and reciprocating motion, Appl. Surf. Sci. 604 (2022) 154538, https://doi.org/10.1016/j.apsusc.2022.154538.
[79] B.J. Hamrock, D. Dowson, Isothermal elastohydrodynamic lubrication of point contacts: Part III—fully flooded results, J. Lubric. Technol. 99 (1977) 264–275, https://doi.org/10.1115/1.3453074.
[80] D. Dowson, Z.-M. Jin, Metal-on-metal hip joint tribology, Proc. Inst. Mech. Eng. H 220 (2006) 107–118, https://doi.org/10.1243/095441105X69114.
[81] C. Kajdas, Importance of anionic reactive intermediates for lubricant component reactions with friction surfaces, Lubric. Sci. 6 (1994) 203–228, https://doi.org/10.1002/ls.3010060302.
[82] M. Kano, Y. Yasuda, Y. Okamoto, Y. Mabuchi, T. Hamada, T. Ueno, J. Ye, S. Konishi, S. Takeshima, J.M. Martin, M.I. De Barros Bouchet, T.L. Mognee, Ultralow friction of DLC in presence of glycerol mono-oleate (GNO), Tribol. Lett. 18 (2005) 245–251, https://doi.org/10.1007/s11249-004-2749-4.
[83] M.I. De Barros Bouchet, M. Kano, 25 - superlubricity of diamond/glycerol technology applied to automotive gasoline engines, in: A. Erdemir, J.-M. Martin (Eds.), Superlubricity, Elsevier Science B.V., Amsterdam, 2007, pp. 471–492, https://doi.org/10.1016/B978-044452772-1/50056-1.
[84] Y. Long, M.-I.D. Barros Bouchet, A. Ristic, N. Dörr, J.M. Martin, Chapter 13 - superlubricity of glycerol is enhanced in the presence of graphene or graphite, in: A. Erdemir, J.M. Martin, J. Luo (Eds.), Superlubricity, second ed., Elsevier, 2021, pp. 231–245, https://doi.org/10.1016/B978-0-444-64313-1.00013-2.
[85] A. Erdemir, Chapter 12 - diamond-like carbon films and their superlubricity, in: A. Erdemir, J.M. Martin, J. Luo (Eds.), Superlubricity, second ed., Elsevier, 2021, pp. 215–230, https://doi.org/10.1016/B978-0-444-64313-1.00012-0.